

Unravelling the emergence of quantum jumps in a monitored qubit

Barkay Guttel,^{1,*} Danielle Gov,^{1,*} Noam Netzer,¹ Uri Goldblatt,¹ Sergey Hazanov,¹ Lalit M. Joshi,¹ Alessandro Romito ,² Yuval Gefen,¹ Parveen Kumar ,³ Kyrylo Snizhko ,⁴ Fabien Lafont,¹ and Serge Rosenblum ,^{1,†}

¹Department of Condensed Matter Physics, Weizmann Institute of Science, Rehovot, Israel

²Department of Physics, Lancaster University, Lancaster LA1 4YB, United Kingdom

³Department of Physics, Indian Institute of Technology Jammu, Jammu 181221, India

⁴Univ. Grenoble Alpes, CEA, Grenoble INP, IRIG, PHELIQS, 38000 Grenoble, France

(Dated: February 4, 2026)

Quantum jumps, the collapse of a quantum system upon measurement, are among the most striking consequences of observation in quantum mechanics. While recent experiments have revealed the continuous nature of individual jumps [1], the crossover from coherent dynamics to measurement-dominated behaviour has remained elusive. Here, we tune the measurement strength of a continuously monitored superconducting qubit, and observe that quantum jumps emerge not through a gradual crossover, but via a cascade of three distinct dynamical transitions [2]. The first transition manifests as an exceptional point [3] where coherent oscillations abruptly cease, giving way to jumps towards a stable eigenstate. The second transition marks the onset of dynamical state freezing, where the qubit's dwell time near the eigenstate diverges. A third threshold signals entry into the quantum Zeno regime, where stronger measurement paradoxically suppresses relaxation [4]. Strikingly, we find that decoherence does not blur these transitions but rather fundamentally restructures the dynamical phase diagram, notably inverting their order. These results map measurement-induced transitions in a monitored qubit, revealing that the interplay between coherent driving, measurement, and decoherence gives rise to a hierarchy of distinct dynamical phases.

A central question in quantum mechanics is how measurement shapes the behaviour of quantum systems. While unobserved systems evolve deterministically under the Schrödinger equation, measurement introduces stochastic evolution [5] through outcome-dependent backaction [6–8]. This tension is particularly striking in a continuously monitored two-level system. Consider a qubit with ground state $|0\rangle$ and excited state $|1\rangle$, driven resonantly at a Rabi rate Ω_S and monitored by a detector that clicks at a rate α when the system is in $|0\rangle$ (Fig. 1). Quantum trajectory theory [9–11] describes how stochastic detector clicks project the system to $|0\rangle$, while between clicks, the wavefunction evolves deterministically under an effective non-Hermitian Hamiltonian (Supplementary Information Section 4) [3, 12, 13]

$$\hat{H}_{\text{eff}}/\hbar = \frac{\Omega_S}{2} (\hat{\sigma}_y - 2i\lambda |0\rangle\langle 0|). \quad (1)$$

Here, the dimensionless measurement strength $\lambda \equiv \alpha/(2\Omega_S)$ quantifies the competition between coherent driving and no-click backaction [14].

The behaviour at the extremes of this parameter is well established. For weak measurements ($\lambda \ll 1$), coherent driving dominates, resulting in Rabi oscillations (Fig. 1). In contrast, for strong measurements ($\lambda \gg 1$), measurement backaction dominates: the sustained absence of clicks drives the qubit towards $|1\rangle$, producing a “continuous quantum jump” [1].

However, the crossover between these two regimes remains experimentally unexplored. A recent theoretical study [2] predicted that this crossover occurs through a cascade of sharp transitions, each unveiling qualitatively distinct dynamics and statistics of quantum trajectories (Fig. 2).

In this work, we provide the first experimental observation of this transition cascade. We realise this using a superconducting circuit consisting of a system qubit coupled to an ancillary detector qubit, forming a V-type three-level system similar to ref. [1]. We control the measurement strength λ by varying the amplitude of a drive

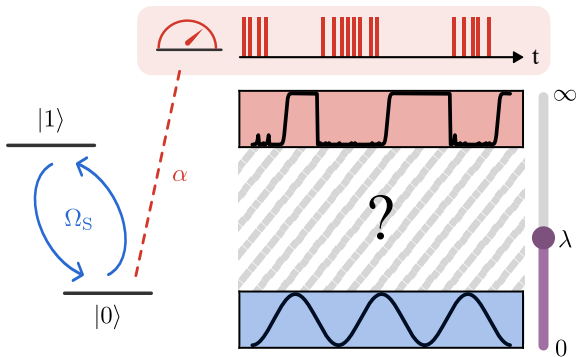


FIG. 1. **Monitored qubit with tunable measurement strength.** The qubit is resonantly driven at a rate Ω_S (blue arrows) while being continuously monitored by a detector. The detector produces clicks (red bars) at a rate α whenever the qubit is in the ground state $|0\rangle$. By tuning the dimensionless measurement strength $\lambda \equiv \alpha/(2\Omega_S)$, we drive a crossover in the qubit dynamics from Rabi oscillations to jump-like trajectories, illustrated by the excited-state population traces (blue and red shaded, respectively).

* These authors contributed equally to this work.

† serge.rosenblum@weizmann.ac.il

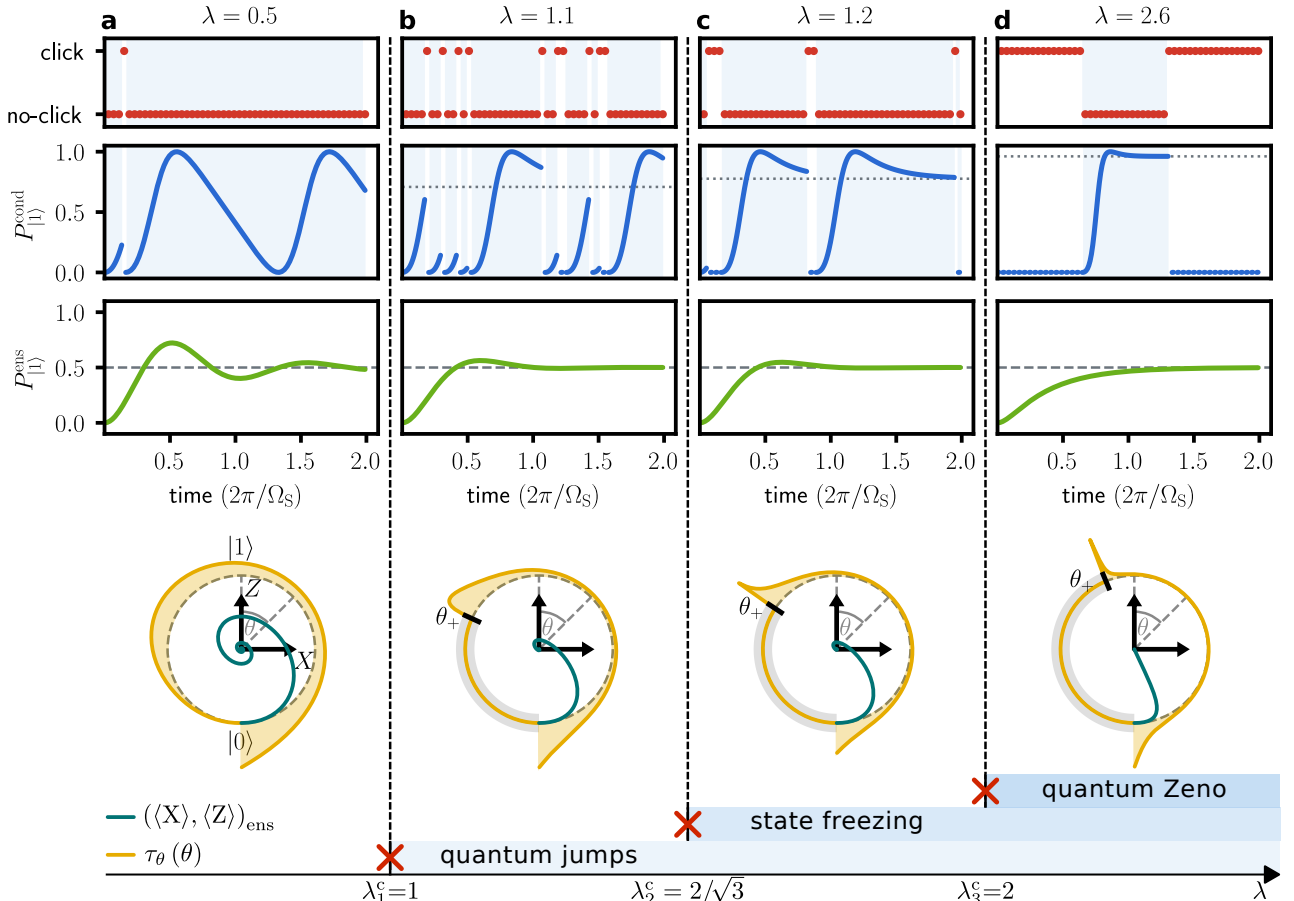


FIG. 2. **Overview of dynamical transitions in the ideal monitored qubit model.** As the dimensionless measurement strength $\lambda \equiv \alpha/(2\Omega_S)$ increases, the qubit dynamics evolve through four distinct regimes (a–d), separated by three sharp transitions at $\lambda_{1-3}^c = \{1, \frac{2}{\sqrt{3}}, 2\}$. Each row displays simulated dynamics in the different regimes, showing (from top to bottom) a representative binary click record, the conditional excited state probability $P_{|1\rangle}^{\text{cond}}$ of the corresponding trajectory, and the ensemble-averaged excited state probability $P_{|1\rangle}^{\text{ens}}$. The Bloch spheres show the average qubit dwell time per unit angle $\tau_\theta(\theta)$ (orange curves), plotted as radial height above the unit circle (a.u.), alongside the time evolution of the ensemble-averaged state initialised at $|0\rangle$ (teal curves). **a**, For $\lambda < \lambda_1^c$, trajectories exhibit periodic Rabi oscillations, intermittently reset to $|0\rangle$ by detector clicks, enabling the qubit to access the full range of polar angles. **b**, The first transition at λ_1^c marks the onset of smooth, deterministic no-click evolution towards a stable eigenstate at polar angle θ_+ (dotted grey lines), creating a forbidden region on the Bloch sphere (grey shading). Detector clicks typically interrupt this no-click evolution before the qubit reaches the eigenstate. **c**, Beyond the second transition ($\lambda > \lambda_2^c$), the qubit frequently reaches and freezes near the eigenstate before a click occurs, resulting in a divergent dwell time at θ_+ . **d**, At the third transition point ($\lambda = \lambda_3^c$), the ensemble-averaged dynamics shift from oscillatory behaviour to overdamped decay with increasingly slow relaxation, marking the onset of quantum Zeno behaviour. In realistic experimental conditions, decoherence modifies both the locations and the ordering of these transitions.

resonant with the detector qubit transition (see Methods). By tuning λ , we uncover three dynamical transitions marking the emergence of measurement-dominated behaviour (Fig. 2). At an exceptional point of the non-Hermitian Hamiltonian, coherent oscillations abruptly cease and trajectories begin evolving towards a stable state—the hallmark of continuous quantum jumps [1, 15]. Beyond a second threshold, the dwell time near this state diverges: trajectories “freeze” in its vicinity. A third transition signals entry into the quantum Zeno regime, where stronger measurement counterintuitively suppresses relaxation [4, 16–18].

Our analysis combines binary detector click records with conditional quantum state tomography. This allows us to reconstruct the qubit’s dynamics conditioned

on specific measurement outcomes, revealing dynamical features that would otherwise be washed out in ensemble averages. Using these methods, we find that decoherence does not merely shift the critical points predicted by the idealised theory, but fundamentally alters the transitions’ character and ordering. Nevertheless, the transitions themselves remain robust features of the dynamics. These results elucidate the emergence of continuous quantum jumps and provide a map of dynamical phases in a monitored qubit.

Transition into the quantum-jump regime

The first transition, heralding the onset of continuous quantum jumps, arises from competition between

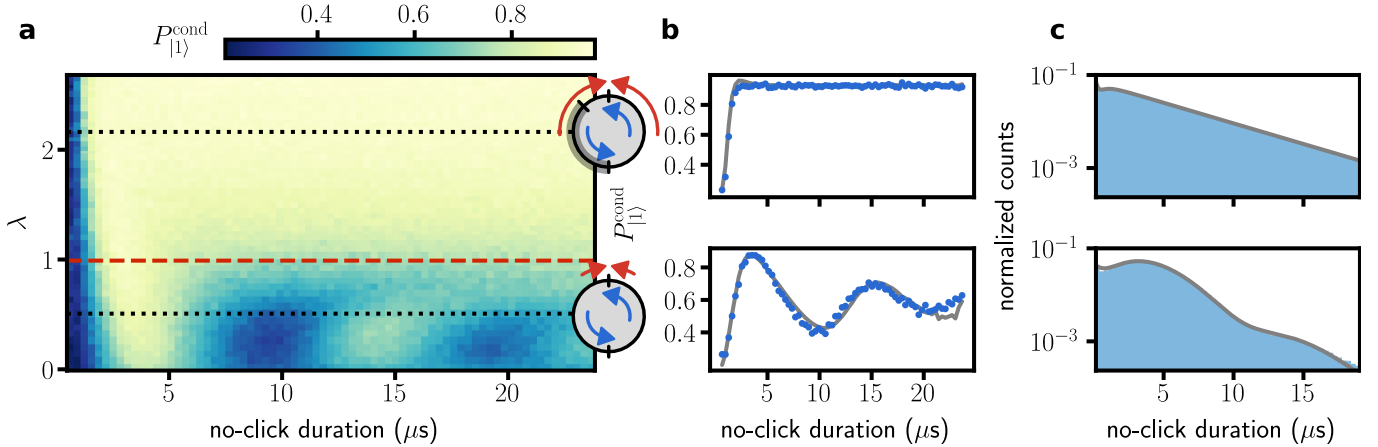


FIG. 3. Observation of the transition to the quantum jump regime. Below the first transition (bottom Bloch sphere), coherent driving (blue arrows) dominates measurement-induced backaction (red arrows) across the entire Bloch sphere, resulting in oscillations. Above it (top Bloch sphere), measurement backaction precisely balances the coherent drive at a specific angle, causing oscillations to halt and giving rise to quantum jump dynamics. **a**, Tomographic data showing the excited state population $P_{|1\rangle}^{\text{cond}}$ as a function of the no-click sequence duration and the measurement strength λ , revealing the shift from oscillatory to jump-like behaviour. The transition is observed at $\lambda_1^{\text{obs}} = 0.99 \pm 0.01$ (dashed red line). Each data point is the average of 1500 experimental runs. **b**, One-dimensional cuts below (bottom panel, $\lambda = 0.5$) and above (top panel, $\lambda = 2.2$) the first transition at λ values indicated by the dotted lines in **a**. The grey lines show the simulated no-click dynamics with independently-measured parameters. Shot-noise error bars are smaller than the marker size. **c**, Histograms of no-click durations further confirm this transition. We initialise the qubit in $|1\rangle$ (in contrast to $|0\rangle$ in **a**, **b**) to suppress the effect of errors in long no-click intervals. The grey solid lines show fits using a sum of three complex exponentials (Methods). Throughout this figure, the single-measurement integration time is $T_{\text{int}} = 320$ ns and the coherent drive strength is set at $\Omega_S/2\pi = 100$ kHz. The tomographic measurement is preceded by a measurement to verify that the system is in the qubit manifold.

two coherent processes acting during no-click evolution (equation (1)): the Rabi drive attempts to rotate the qubit around the Bloch sphere, while the no-click measurement backaction pulls it towards the excited state $|1\rangle$. Below a critical measurement strength $\lambda < \lambda_1^c$, Rabi driving dominates at all polar angles θ on the Bloch sphere, allowing the qubit to complete full periodic rotations. As λ approaches λ_1^c , the oscillations become increasingly asymmetric, reflecting the growing impact of measurement backaction (Fig. 2a). The critical point $\lambda_1^c = 1$ represents the threshold at which measurement backaction first becomes strong enough to halt the qubit's rotation. For any $\lambda \geq \lambda_1^c$, backaction precisely balances coherent driving at an angle $\theta_+(\lambda) = 2 \arctan(\sqrt{\lambda^2 - 1} - \lambda)$, creating a stable fixed point¹ [19]. Trajectories now execute continuous, deterministic quantum jumps from $|0\rangle$ towards the eigenstate of \hat{H}_{eff} , $|\psi_+\rangle \equiv \sin\left(\frac{\theta_+}{2}\right)|0\rangle + \cos\left(\frac{\theta_+}{2}\right)|1\rangle$, until a stochastic detector click resets the qubit to $|0\rangle$. The fixed point at $|\psi_+\rangle$ creates a forbidden region $(-\pi, \theta_+(\lambda)]$ on the Bloch sphere, which eventually encompasses the entire left hemisphere as measurement strength increases [2] (see the Bloch spheres in Figs. 2b–d).

This transition coincides with an exceptional point —

a degeneracy in the spectrum of the non-Hermitian no-click Hamiltonian \hat{H}_{eff} where eigenvalues coalesce. Since the Hamiltonian is parity-time (\mathcal{PT}) symmetric, the exceptional point separates unbroken and broken \mathcal{PT} -symmetric phases [13]. Beyond this point, the eigenvalue difference becomes purely imaginary, causing the oscillation frequency to vanish. Similar exceptional-point transitions have been observed in other systems [3, 20–24].

To observe this transition experimentally, we reconstruct the qubit's evolution conditioned on the absence of detector clicks. We perform qubit tomography after detecting in real time a no-click sequence of the desired duration. Repeating this procedure across different no-click durations and measurement strengths reveals a clear shift from oscillatory to quantum jump dynamics (Figs. 3a,b). The measurements are in excellent agreement with numerical simulations of a model that incorporates decoherence (Supplementary Information Section 8). As expected, the Rabi oscillations become increasingly distorted as λ approaches the critical value.

The distribution of no-click durations independently confirms this transition. Initialising the system in $|1\rangle$, we record the waiting time to the first detector click. Since the instantaneous click rate varies as $r(\theta) \equiv \alpha \sin^2\left(\frac{\theta(t)}{2}\right)$, Rabi oscillations imprint a periodic modulation on this distribution. The data (Fig. 3c) confirm this expectation: oscillatory patterns at weak measurements give way to monotonic decay as λ increases. From the vanishing of oscillations, we determine that the transition to quantum-jump dynamics occurs at $\lambda_1^{\text{obs}} = 0.99 \pm 0.01$

¹ A second fixed point appears at $\theta_- \equiv -\pi - \theta_+$ [2]. However, this fixed point is unstable, so the qubit reaches it only if specifically initialised in that state.

(Methods and Supplementary Information Section 7).

Transition into the state-freezing regime

A defining feature of strongly measured quantum systems is dynamical freezing: the qubit should not merely approach the eigenstate $|\psi_+\rangle$ but remain trapped in its vicinity for extended periods. To probe this behaviour, we examine the dwell time per unit angle $\tau_\theta(\theta)$, defined such that $\tau_\theta(\theta)\Delta\theta$ gives the mean time spent in the angular interval $[\theta, \theta + \Delta\theta]$. Near the fixed point at θ_+ , theory predicts a power-law scaling $\tau_\theta(\theta) \sim [\theta - \theta_+(\lambda)]^{\xi(\lambda)}$ [2], where the sign of the critical exponent ξ reflects a competition between the click rate and the rate at which trajectories approach θ_+ . When clicks dominate ($\xi > 0$), the dwell time vanishes at the fixed point (Fig. 2b). When the approach rate dominates ($\xi < 0$), trajectories accumulate faster than clicks can reset them, and the dwell time diverges (Fig. 2c). This sign change defines a second critical threshold at $\lambda_2^c = \frac{2}{\sqrt{3}} \approx 1.15$ in the ideal model (Supplementary Information Section 4), marking the onset of dynamical state freezing.

We reconstruct $\tau_\theta(\theta)$ experimentally by initialising the qubit in $|1\rangle$, recording the angular distribution $\rho(\theta)$ of first-click events, and normalising by the instantaneous click rate $r(\theta)$ (Methods and Supplementary Information Section 4). Fig. 4a shows the resulting dwell-time distributions across a range of measurement strengths. For weak measurement strengths ($\lambda \ll 1$), the qubit completes full Rabi oscillations and $\tau_\theta(\theta)$ is approximately uniform. As λ increases, a forbidden angular region emerges. Intriguingly, this occurs at $\lambda \approx 0.57$, well before oscillations cease at $\lambda_1^{\text{obs}} = 0.99$. This decoupling of the two signatures of the first transition is absent in the ideal model, where both appear simultaneously at $\lambda_1^c = 1$. We attribute this discrepancy to decoherence, which causes the qubit's no-click trajectory to spiral into the Bloch sphere's interior. This altered trajectory permits a forbidden region and a fixed point to exist in the presence of damped oscillations.

At higher measurement strengths, a pronounced peak develops at the fixed point, consistent with the predicted divergence. By fitting $\tau_\theta(\theta)$ to the expected power law and extracting the zero crossing of ξ (Fig. 4b), we locate the second transition at $\lambda_2^{\text{obs}} = 0.92 \pm 0.01$ (Methods and Supplementary Information Section 7). Strikingly, this lies *below* the first transition, inverting the prediction of the ideal model. This counterintuitive result again reflects the influence of decoherence: analytical and numerical calculations show that decoherence shifts the second transition to lower λ while raising the first, causing them to cross (Fig. 6 and Supplementary Information Section 6).

Transition into the quantum Zeno regime

The third and final transition occurs when the system enters the quantum Zeno regime [2, 25]. Beyond this

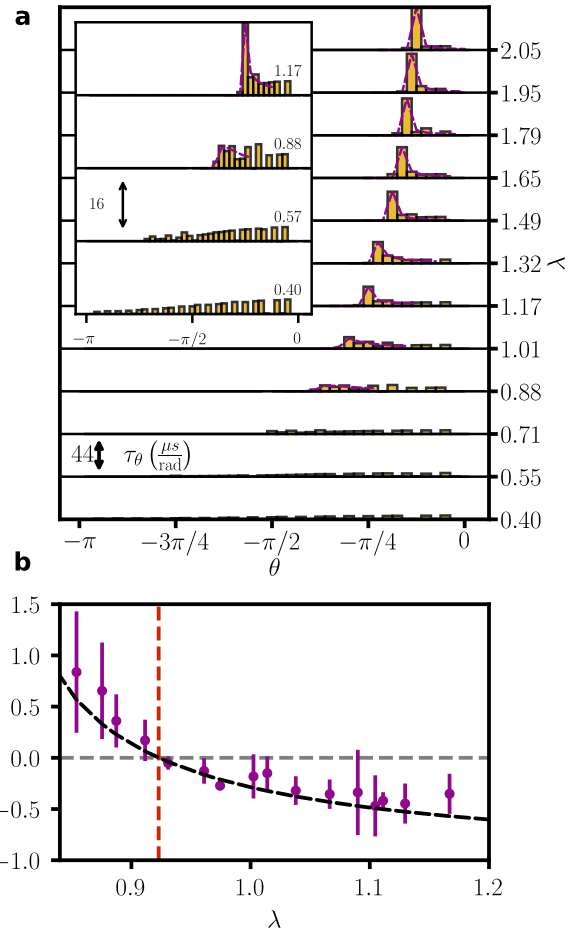


FIG. 4. Dwell time per unit angle $\tau_\theta(\theta)$ across the second transition. **a**, Ridge plot showing how the dwell time evolves with measurement strength λ . Purple dashed lines are fits to the analytical model $\tau_\theta(\theta) \sim [\theta - \theta_+(\lambda)]^{\xi(\lambda)}$ (Methods), performed only when $\theta_+ > -\pi/2$. **Inset:** zoom-in on four representative values of λ illustrating the transition: at $\lambda = 0.4$, the dwell time is nonzero across all angles; at $\lambda = 0.57$, a forbidden region has formed, before the first transition at λ_1^{obs} ; at $\lambda = 0.88$, the dwell time remains small near θ_+ ; at $\lambda = 1.17$, a pronounced peak develops. Vertical arrows in both the main panel and the inset indicate the scale. **b**, Fitted critical exponent ξ versus λ . Error bars represent 1σ confidence intervals. The dashed black line is a fit to the analytical model, yielding $\lambda_2^{\text{obs}} = 0.92 \pm 0.01$ (vertical red line) at $\xi = 0$ (horizontal grey line), marking the transition from finite to diverging dwell time near the forbidden region. Throughout, the coherent drive is $\Omega_S/2\pi = 100$ kHz and the angular bin width is $2\pi/80$.

transition point, measurement-induced backaction suppresses, rather than accelerates, the relaxation of the initial state towards the steady state [4, 26–28] (Figs. 2c,d). In addition, measurement-induced dephasing critically damps the ensemble dynamics at the transition point, turning decaying oscillations into an overdamped decay of the qubit polarisation. These changes stem from an exceptional point of the Liouvillian superoperator \mathcal{L} in the master equation for the qubit's density matrix

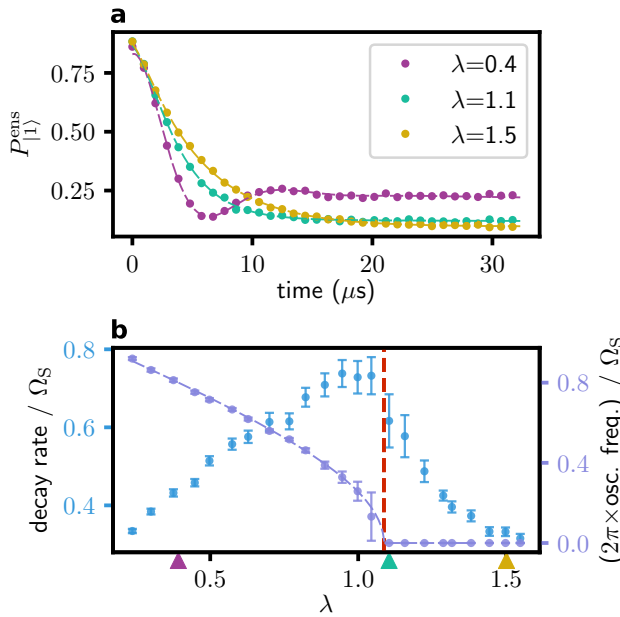


FIG. 5. Relaxation to the steady state across the third transition. At this transition, oscillatory decay gives way to overdamped relaxation; beyond it, stronger measurement slows relaxation, marking entry into the quantum Zeno regime. **a**, Ensemble-averaged excited state probability $P_{|1\rangle}^{\text{ens}}$ for selected λ . Each data point is the average of 3000 experimental runs. Error bars are smaller than the marker size. Dashed lines show fits using a sum of three complex exponentials. **b**, Extracted relaxation rates (blue) and oscillation frequencies (purple) versus λ . Error bars indicate 1σ confidence intervals. The dashed line is a fit of the oscillation frequency to the predicted behaviour (Methods). The transition is observed at $\lambda_3^{\text{obs}} = 1.09 \pm 0.01$ (dashed red line), below the ideal value $\lambda_3^{\text{c}} = 2$ owing to finite waiting time in the detector’s excited state. Throughout, the coherent drive is $\Omega_S/2\pi = 100$ kHz.

$\hat{\rho}(t)$ [29, 30],

$$\dot{\hat{\rho}} = \mathcal{L}\hat{\rho} = -i \left[\frac{\Omega_S}{2} \hat{\sigma}_y, \hat{\rho}(t) \right] + \alpha \mathcal{D} [|0\rangle\langle 0|] \hat{\rho}(t), \quad (2)$$

with the dissipator $\mathcal{D}[\hat{L}](\hat{\rho}) = \hat{L}\hat{\rho}\hat{L}^\dagger - \frac{1}{2} \left\{ \hat{L}^\dagger \hat{L}, \hat{\rho} \right\}$ capturing both the stochastic clicks generated by $\hat{L} = |0\rangle\langle 0|$ and the no-click backaction generated by $\hat{L}^\dagger \hat{L}$.

To probe this transition, we perform state tomography after variable evolution times without conditioning on the click record (Fig. 5a). For small λ , the decay rate grows monotonically with λ , while the oscillation frequency decreases (Fig. 5b). However, at the observed transition point $\lambda_3^{\text{obs}} = 1.09 \pm 0.01$ (Methods), the dynamics become overdamped and oscillations vanish. Beyond this point, further increasing λ slows down the exponential decay, completing the entry into the quantum Zeno regime [2]. The observed transition lies well below the ideal prediction $\lambda_3^{\text{c}} = 2$ owing to the finite waiting time τ_B in the detector’s excited state between a click and the start of

a new trajectory. This waiting time renders the dynamics partially non-Hermitian, lowering the critical value (Supplementary Information Section 6 D) [31].

Conclusions

The transition from drive-dominated coherent evolution to measurement-dominated behaviour manifests not as a gradual crossover, but as a discrete cascade of dynamical phases. By accessing the full measurement record, we resolve these transitions individually, each revealing a distinct hallmark of monitored quantum systems that is obscured in ensemble averages. Strikingly, decoherence does not blur these transitions but fundamentally restructures the dynamical phase diagram (Fig. 6), inverting the ordering of the first two critical points: dephasing shifts the state-freezing threshold below the onset of continuous quantum jumps, while the detector’s finite waiting time lowers the onset of quantum Zeno dynamics (Supplementary Information Section 5). Additional probes—such as click counting fields [25] or trajectory-resolved entropy production [32]—may uncover further structure, including topologically distinct phases [25, 33]. More broadly, the cascaded emergence of measurement-induced dynamics should extend beyond the single-qubit setting, with implications for measurement-enhanced entanglement generation [34] and measurement-induced phase transitions in many-body systems [35–38].

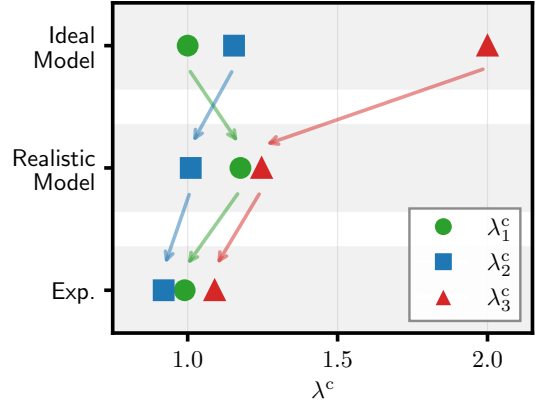


FIG. 6. Summary of transition locations. Comparison of the three critical measurement strengths $\lambda_{1,2,3}^c$ across three levels of description: the ideal model ($\lambda_1^c = 1$, $\lambda_2^c = 2/\sqrt{3}$, $\lambda_3^c = 2$), the realistic model (Supplementary Information Section 5) incorporating decoherence ($\lambda_1^c = 1.18$, $\lambda_2^c = 1.01$, $\lambda_3^c = 1.25$), and experimental observations ($\lambda_1^{\text{obs}} = 0.99$, $\lambda_2^{\text{obs}} = 0.92$, $\lambda_3^{\text{obs}} = 1.09$). Notably, decoherence inverts the ordering of the first two transitions ($\lambda_2^c < \lambda_1^c$), a feature captured by the realistic model. Remaining discrepancies likely reflect residual systematics in calibration and data analysis (Supplementary Information Section 7).

[1] Minev, Z. K. *et al.* To catch and reverse a quantum jump mid-flight. *Nature* **570**, 200–204 (2019).

[2] Snizhko, K., Kumar, P. & Romito, A. Quantum Zeno effect appears in stages. *Physical Review Research* **2**, 033512 (2020).

[3] Naghiloo, M., Abbasi, M., Joglekar, Y. N. & Murch, K. W. Quantum state tomography across the exceptional point in a single dissipative qubit. *Nature Physics* **15**, 1232–1236 (2019).

[4] Greenfield, S., Kamal, A., Dressel, J. & Levenson-Falk, E. A unified picture for quantum Zeno and anti-Zeno effects (2025). ArXiv:2506.12679 [quant-ph].

[5] Dalibard, J., Castin, Y. & Mølmer, K. Wave-function approach to dissipative processes in quantum optics. *Physical Review Letters* **68**, 580–583 (1992).

[6] Hatridge, M. *et al.* Quantum back-action of an individual variable-strength measurement. *Science* **339**, 178–181 (2013).

[7] Weber, S. J., Murch, K. W., Kimchi-Schwartz, M. E., Roch, N. & Siddiqi, I. Quantum trajectories of superconducting qubits. *Comptes Rendus Physique* **17**, 766–777 (2016).

[8] Murch, K. W., Weber, S. J., Macklin, C. & Siddiqi, I. Observing single quantum trajectories of a superconducting quantum bit. *Nature* **502**, 211–214 (2013).

[9] Carmichael, H. J. Quantum trajectory theory for cascaded open systems. *Physical Review Letters* **70**, 2273–2276 (1993).

[10] Mølmer, K., Castin, Y. & Dalibard, J. Monte Carlo wavefunction method in quantum optics. *Journal of the Optical Society of America B* **10**, 524–538 (1993).

[11] Wiseman, H. M. Quantum trajectories and quantum measurement theory. *Quantum and Semiclassical Optics: Journal of the European Optical Society Part B* **8**, 205 (1996).

[12] Ashida, Y., Gong, Z. & Ueda, M. Non-Hermitian physics. *Advances in Physics* **69**, 249–435 (2020).

[13] Bender, C. M. Making sense of non-Hermitian Hamiltonians. *Reports on Progress in Physics* **70**, 947–1018 (2007).

[14] Remminger, M. Messungen ohne Störung des Meßobjekts. *Zeitschrift für Physik* **158**, 417–421 (1960).

[15] Katz, N. *et al.* Coherent state evolution in a superconducting qubit from partial-collapse measurement. *Science* **312**, 1498–1500 (2006).

[16] Peres, A. Zeno paradox in quantum theory. *American Journal of Physics* **48**, 931–932 (1980).

[17] Misra, B. & Sudarshan, E. C. G. The zeno's paradox in quantum theory. *Journal of Mathematical Physics* **18**, 756–763 (1976).

[18] Gambetta, J. *et al.* Quantum trajectory approach to circuit QED: Quantum jumps and the Zeno effect. *Physical Review A* **77**, 012112 (2008).

[19] Ruskov, R., Mizel, A. & Korotkov, A. N. Crossover of phase qubit dynamics in the presence of a negative-result weak measurement. *Physical Review B* **75**, 220501 (2007).

[20] Wu, Y. *et al.* Observation of parity-time symmetry breaking in a single-spin system. *Science* **364**, 878–880 (2019).

[21] Ding, L. *et al.* Experimental determination of PT-symmetric exceptional points in a single trapped ion. *Physical Review Letters* **126**, 083604 (2021).

[22] Dogra, S., Melnikov, A. A. & Paraoanu, G. S. Quantum simulation of parity-time symmetry breaking with a superconducting quantum processor. *Communications Physics* **4**, 26 (2021).

[23] Wang, W.-C. *et al.* Observation of PT-symmetric quantum coherence in a single-ion system. *Physical Review A* **103**, L020201 (2021).

[24] Hu, L. *et al.* Full-parameter-space quantum simulation of high-fidelity PT-symmetric dynamics in a trapped ion. *Physical Review A* **112**, 052611 (2025).

[25] Li, F., Ren, J. & Sinitsyn, N. A. Quantum Zeno effect as a topological phase transition in full counting statistics and spin noise spectroscopy. *Europhysics Letters* **105**, 27001 (2014).

[26] Kakuyanagi, K. *et al.* Observation of quantum Zeno effect in a superconducting flux qubit. *New Journal of Physics* **17**, 063035 (2015).

[27] Xiao, L. & Jones, J. A. NMR analogues of the quantum Zeno effect. *Physics Letters A* **359**, 424–427 (2006).

[28] Palacios-Laloy, A. *et al.* Experimental violation of a Bell's inequality in time with weak measurement. *Nature Physics* **6**, 442–447 (2010).

[29] Minganti, F., Miranowicz, A., Chhajlany, R. W. & Nori, F. Quantum exceptional points of non-Hermitian Hamiltonians and Liouvillians: The effects of quantum jumps. *Physical Review A* **100**, 062131 (2019).

[30] Dubey, V., Chetrite, R. & Dhar, A. Quantum resetting in continuous measurement induced dynamics of a qubit. *Journal of Physics A: Mathematical and Theoretical* **56**, 154001 (2023).

[31] Minganti, F., Miranowicz, A., Chhajlany, R. W., Arkhipov, I. I. & Nori, F. Hybrid-Liouvillian formalism connecting exceptional points of non-Hermitian Hamiltonians and Liouvillians via postselection of quantum trajectories. *Physical Review A* **101**, 062112 (2020).

[32] Harrington, P. M., Tan, D., Naghiloo, M. & Murch, K. W. Characterizing a statistical arrow of time in quantum measurement dynamics. *Physical Review Letters* **123**, 020502 (2019).

[33] Pavlov, A. I., Gefen, Y. & Shnirman, A. Topological transitions in quantum jump dynamics: Hidden exceptional points. *Physical Review B* **111**, 104301 (2025).

[34] Li, Z.-Z., Chen, W., Abbasi, M., Murch, K. W. & Whaley, K. B. Speeding up entanglement generation by proximity to higher-order exceptional points. *Physical Review Letters* **131**, 100202 (2023).

[35] Skinner, B., Ruhman, J. & Nahum, A. Measurement-induced phase transitions in the dynamics of entanglement. *Physical Review X* **9**, 031009 (2019).

[36] Li, Y., Chen, X. & Fisher, M. P. A. Quantum Zeno effect and the many-body entanglement transition. *Physical Review B* **98**, 205136 (2018).

[37] Szyniszewski, M., Romito, A. & Schomerus, H. Entanglement transition from variable-strength weak measurements. *Physical Review B* **100**, 064204 (2019).

[38] Fisher, M. P. A., Khemani, V., Nahum, A. & Vijay, S. Random quantum circuits. *Annual Review of Condensed Matter Physics* **14**, 335–379 (2023).

[39] Mundada, P., Zhang, G., Hazard, T. & Houck, A. Suppression of qubit crosstalk in a tunable coupling super-

conducting circuit. *Physical Review Applied* **12**, 054023 (2019).

[40] Slichter, D. H. *et al.* Quantum Zeno effect in the strong measurement regime of circuit quantum electrodynamics. *New Journal of Physics* **18**, 053031 (2016).

[41] Baum, L. E., Petrie, T., Soules, G. & Weiss, N. A maximization technique occurring in the statistical analysis of probabilistic functions of Markov chains. *The Annals of Mathematical Statistics* **41**, 164–171 (1970).

[42] Sarkar, T. K. & Pereira, O. Using the matrix pencil method to estimate the parameters of a sum of complex exponentials. *IEEE Antennas and Propagation Magazine* **37**, 48–55 (1995).

[43] Blais, A., Grimsmo, A. L., Girvin, S. M. & Wallraff, A. Circuit quantum electrodynamics. *Reviews of Modern Physics* **93**, 025005 (2021).

[44] Sank, D. *et al.* System characterization of dispersive readout in superconducting qubits. *Physical Review Applied* **23**, 024055 (2025).

[45] Yuzhelevski, Y., Yuzhelevski, M. & Jung, G. Random telegraph noise analysis in time domain. *Review of Scientific Instruments* **71**, 1681–1688 (2000).

[46] Welters, A. On explicit recursive formulas in the spectral perturbation analysis of a Jordan block. *SIAM Journal on Matrix Analysis and Applications* **32**, 1–22 (2011).

METHODS

Experimental setup. Our device comprises two fixed-frequency transmon qubits housed in a 3D superconducting readout cavity [1]. The system or “dark” qubit is oriented perpendicularly to the field of the cavity’s fundamental mode, causing a weak dispersive shift of $\chi_S/2\pi = 0.27$ MHz. By contrast, the detector or “bright” qubit is aligned parallel to the field and couples an order of magnitude more strongly to the cavity ($\chi_B/2\pi = 5.1$ MHz). Due to the nonlinear interaction between the two qubits [39], the doubly excited state $|e_S, e_B\rangle$ is shifted by $\chi_{SB}/2\pi = 36$ MHz and becomes inaccessible, leaving an effective V-shaped three-level system: the ground state $|0\rangle \equiv |g_S, g_B\rangle$, the dark excited state $|1\rangle \equiv |e_S, g_B\rangle$ (system qubit excitation), and the bright excited state $|B\rangle \equiv |g_S, e_B\rangle$ (detector qubit excitation).

By applying a readout tone at $\omega = \omega_R - \chi_B$, with ω_R the readout cavity frequency, we monitor the population in $|B\rangle$ at a rate $\Gamma \propto \bar{n}_B$, with \bar{n}_B the average number of readout photons set by the readout tone amplitude Ω_R . Due to the large asymmetry in the dispersive shifts, we achieve rapid, single-shot readout distinguishing $|B\rangle$ from $|0\rangle$ and $|1\rangle$ with a fidelity exceeding 95% within an integration time $T_{\text{int}} = 320$ ns. A weak resonant drive of amplitude $\Omega_B \ll \Gamma$ induces excursions from $|0\rangle$ to $|B\rangle$, producing detector “clicks” at rate $\alpha \propto \Omega_B^2/\Gamma$ [40]. To tune λ , we adjust Ω_B while keeping the system drive Ω_S and the readout tone Ω_R fixed. More details on the experimental setup can be found in Supplementary Information Sections 1 and 2.

Calibration of the measurement rate α . The click rate α is defined as the inverse of the mean waiting time the qubit spends in $|0\rangle$ (with $\Omega_S = 0$) before being excited to the detector’s excited state $|B\rangle$, where it produces a detector click. We determine α from a hidden Markov model (HMM) analysis of the detector click record. In this approach, we use the Baum–Welch algorithm [41] to infer the underlying transition rate α from $|0\rangle$ to $|B\rangle$ using the observed click sequence. This independently calibrated rate determines the dimensionless measurement strength via the relation $\lambda = \alpha/(2\Omega_S)$. In addition to the measurement rate, the HMM analysis also provides the waiting time τ_B in $|B\rangle$. More details are provided in Supplementary Information Section 3.

Quantum state tomography. Quantum state tomography at the end of an experimental run occurs either after a preset duration or conditioned on detection of a specific click pattern. After switching off all three drives, a first projective measurement verifies that the system is not in the detection state $|B\rangle$. Conditioned on finding the system within the qubit manifold $\{|0\rangle, |1\rangle\}$, a set of calibrated Pauli operations maps the X, Y, or Z polarisations of the system manifold onto the detection manifold $\{|0\rangle, |B\rangle\}$. A second projective measurement is then performed, enabling reconstruction of the system’s density matrix.

Constructing angular dwell time histograms. To reconstruct the angular dwell time distribution $\tau_\theta(\theta)$, we use two measured quantities: the temporal probability density of the first click $\rho(t)$ and the instantaneous click rate $r(t) = -[dP^{(0)}(t)/dt]/P^{(0)}(t)$, where $P^{(0)}(t)$ is the no-click probability up to time t . Using the angular no-click evolution $\theta(t)$ obtained from quantum state tomography, these quantities are converted to their angular counterparts, $\rho(\theta)$ and $r(\theta)$. The mean dwell time per unit angle in the interval $[\theta, \theta + \Delta\theta]$ is then calculated as:

$$\tau_\theta(\theta) = \frac{\rho(\theta)}{r(\theta)},$$

as detailed in Supplementary Information Section 4.

Because the boundary of the forbidden region can land arbitrarily close to a bin edge, we employ a deterministic rule to avoid numerical artefacts. For each λ in Fig. 4, we compute two histograms from the same data: one on a grid starting at $-\pi$ and one shifted by half a bin width. We then select the grid that yields the larger single-bin dwell time within the window $(-\frac{\pi}{2}, 0)$, where the divergence is expected. For $\lambda \leq \lambda_2^c$, the choice has no perceptible effect, while for $\lambda > \lambda_2^c$ it preserves the visibility of the divergence at θ_+ .

Extracting the observed transition locations λ_1^{obs} . To extract λ_1^{obs} , we analyse the dynamics of $P^{(0)}(t)$, which is described by a sum of three complex exponentials corresponding to three poles in the Laplace domain (Supplementary Information Section 6 A). Using the matrix pencil method [42], we estimate these poles and track e_1, e_2 , which form a complex-conjugate pair below the transition. The transition occurs when this pair coalesces and splits into two distinct real values. We extract λ_1^{obs} by fitting the pole splitting $\Delta e_{12} = (e_1 - e_2)/2$ near the transition to

$$\Delta e_{12} = a(\lambda - \lambda_1^{\text{obs}})^{0.5} + b(\lambda - \lambda_1^{\text{obs}})^{1.5}, \quad (3)$$

a functional form derived from the square-root singularity characteristic of exceptional points (Supplementary Information Section 7). Uncertainties are estimated using a residual bootstrap procedure.

To extract λ_2^{obs} , we analyse the angular dwell time data in Fig. 4. The data are fitted to the binned version of the analytical form of the angular dwell time (Supplementary Information Section 4):

$$\tau_\theta(\theta | A, \theta_+, \xi) = \begin{cases} \frac{A (\tan \frac{\theta}{2} - \tan \frac{\theta_+}{2})^\xi}{\cos^4 \frac{\theta}{2} (\tan \frac{\theta}{2} - \cot \frac{\theta_+}{2})^{\xi+4}} & \theta_+ \leq \theta \leq 0, \\ 0 & \text{otherwise,} \end{cases} \quad (4)$$

with

$$\xi = (\lambda / \sqrt{\lambda^2 - 1}) - 2. \quad (5)$$

For $\xi > 0$, τ_θ vanishes as $[\theta - \theta_+]^\xi$ when $\theta \rightarrow \theta_+$, while for $-1 < \xi < 0$ it diverges. We fit this expression near

the first non-vanishing bin (approximately θ_+), treating θ_+ , ξ , and the scaling parameter A as independent parameters. We then fit $\xi(\lambda)$ to equation (5), allowing only a horizontal shift. The transition point is identified by $\xi(\lambda_2^{\text{obs}}) = 0$. Further details and full-scan fits are provided in Supplementary Information Section 7.

To extract λ_3^{obs} , we apply the same pole-based procedure used for λ_1^{obs} to the ensemble-averaged excited state probability $P_{|1\rangle}^{\text{ens}}$ shown in Fig. 5a. Although $P_{|1\rangle}^{\text{ens}}$ is described by a sum of four complex exponentials (Supplementary Information Section 6 D), numerical analysis indicates that one eigenmode decays faster than the time resolution set by the integration time T_{int} and is therefore not resolvable. The matrix pencil model-order selection confirms three resolvable poles in the relevant λ range. The difference between e_1 and e_2 , the two poles in the conjugate pair, is fitted to the functional form in equation (3), replacing λ_1^{obs} with λ_3^{obs} . For details, see Supplementary Information Section 7.

ADDITIONAL INFORMATION

Correspondence and requests for materials should be addressed to Serge Rosenblum.

Competing interests: The authors declare no competing interests.

Data availability: The data that support the findings of this study are available from the corresponding authors on request.

Code availability: The code related to the data analysis of this study is available from the corresponding authors on request.

ACKNOWLEDGMENTS

We thank Nissim Ofek for his contribution to implementing the real-time tomography experiment, and acknowledge Barak Dayan, Eran Sela, and Kater Murch for their feedback on this manuscript. We acknowledge financial support from the Israel Science Foundation (ISF) Grant no. 2166/25. This work is part of the HQI (www.hqi.fr) and BACQ initiatives and is supported by the France 2030 program under the French National Research Agency grants with numbers ANR-22-PNCQ-0002 and ANR-22-QMET-0002 (MetriQs-France). P.K. acknowledges support from the IIT Jammu Initiation Grant No. SGT-100106. Y.G. was supported by the Deutsche Forschungsgemeinschaft (DFG) grant SH 81/8-1 and by the National Science Foundation (NSF-2338819) and Binational Science Foundation (BSF-2023666). S.R. is the incumbent of the Rabbi Dr. Roger Herst Career Development Chair.

AUTHOR CONTRIBUTIONS

B.G. and D.G. designed and performed the experiments. B.G., D.G., and N.N. analysed data and performed numerical simulations. L.M.J. performed the device fabrication. U.G. and S.H. developed code for the experiments. P.K., A.R., K.S., and Y.G. developed the theory. B.G., D.G., N.N., K.S., A.R., P.K., Y.G., and S.R. wrote the manuscript, with input from all authors. Y.G., F.L., K.S., and S.R. conceived and supervised the project.

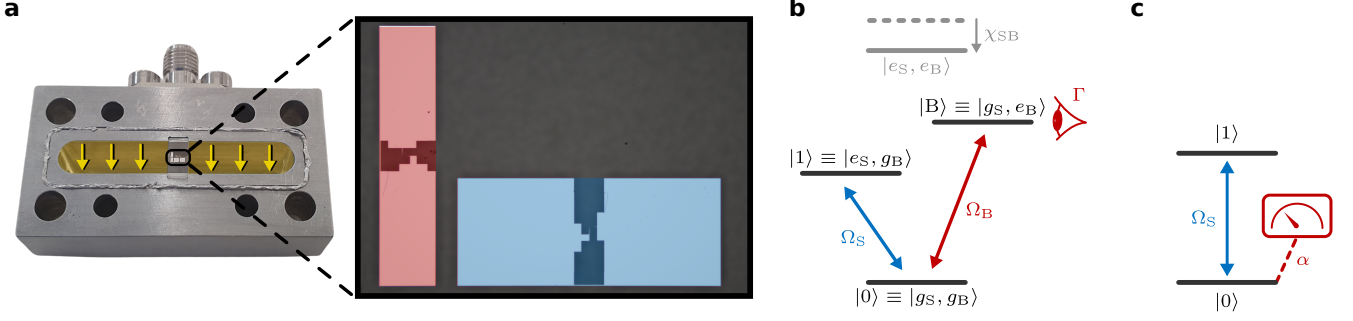


FIG. S1. **Experimental implementation of a qubit with tunable monitoring strength.** **a**, Two-transmon chip mounted within a rectangular 3D superconducting cavity. In the expanded view, the detector (“bright”) transmon (red) is aligned with the cavity field lines (yellow arrows) to ensure strong dispersive coupling. The system (“dark”) transmon (blue) is oriented perpendicular to the field, strongly suppressing its dispersive coupling to the readout mode. **b**, Energy level diagram showing the shared ground state $|0\rangle$ and two single-excitation states $|1\rangle$ and $|B\rangle$ forming a V-type structure. Higher-excitation states (e.g., the doubly excited state, shown in grey) lie outside the operating manifold. A resonant drive of amplitude Ω_B couples $|0\rangle$ to $|B\rangle$, whose population is continuously monitored via the readout cavity at rate Γ . **c**, This configuration effectively realises a two-level system whose ground state is continuously monitored by a click detector with tunable measurement strength $\alpha \propto \Omega_B^2/\Gamma$.

SI 1: Experimental System

The device consists of two fixed-frequency transmon qubits housed in a three-dimensional superconducting readout cavity [1]. The chip was fabricated on a 430-μm-thick sapphire substrate using electron-beam lithography. Aluminium was deposited in two orthogonal evaporation with an in situ oxidation step between them to form Manhattan-style Al/AlO_x/Al tunnel junctions. The chip is placed in a rectangular 1060 aluminium cavity (Fig. S1a), whose fundamental mode serves as the readout resonance. The cavity halves were etched and sealed with indium wire to improve the internal quality factor. The two transmon qubits are oriented to achieve strongly asymmetric dispersive coupling to the readout mode: the detector (“bright”) qubit is aligned parallel to the cavity field, maximising the dispersive coupling ($\chi_B/2\pi = 5.1$ MHz). This enables rapid, high-fidelity readout of the detector’s excited state $|B\rangle$. The system (“dark”) qubit is oriented perpendicularly to the cavity field, strongly suppressing its dispersive coupling ($\chi_S/2\pi = 0.27$ MHz). This minimises measurement-induced dephasing of the system qubit.

The nonlinear interaction between the two qubits shifts the doubly excited state $|e_S, e_B\rangle$ by $\chi_{SB}/2\pi = 36$ MHz, rendering it inaccessible under resonant driving. This leaves an effective V-shaped three-level system (Fig. S1b).

The cavity is enclosed within successive Amumetal and OFHC copper shields for magnetic and thermal isolation, and mounted on the mixing-chamber stage of a dilution refrigerator with base temperature of ~ 10 mK. The full wiring diagram is shown in Fig. S9.

SI 2: System Parameters

The complete Hamiltonian describing the two transmons and readout cavity (in the absence of drives) is:

$$\hat{H}_{\text{full}}/\hbar = \omega_B \hat{b}^\dagger \hat{b} - \frac{K_B}{2} \hat{b}^\dagger \hat{b}^2 + \omega_S \hat{s}^\dagger \hat{s} - \frac{K_S}{2} \hat{s}^\dagger \hat{s}^2 - \chi_{SB} \hat{b}^\dagger \hat{b} \hat{s}^\dagger \hat{s} + (\omega_R - \chi_B \hat{b}^\dagger \hat{b} - \chi_S \hat{s}^\dagger \hat{s}) \hat{r}^\dagger \hat{r}, \quad (\text{S1})$$

where \hat{b} , \hat{s} , and \hat{r} are the annihilation operators for the detector transmon, system transmon, and readout cavity modes, respectively. The parameters for this Hamiltonian, along with relevant coherence properties, are detailed in Table S1.

SI 3: Measurement Scheme

This section describes how we continuously monitor the qubit and extract the measurement rate α from the recorded data.

parameter	description	value
ω_S	system qubit resonance frequency	$2\pi \times 5.393$ GHz
K_S	system qubit anharmonicity	$2\pi \times 146$ MHz
T_S^1	system qubit lifetime	$93\ \mu\text{s}$
T_S^2	system qubit coherence time	$23\ \mu\text{s}$
χ_S	system qubit-cavity dispersive shift	$2\pi \times 0.27$ MHz
n_S^{th}	system qubit average thermal population	3.5%
ω_B	detector qubit resonance frequency	$2\pi \times 6.265$ GHz
K_B	detector qubit anharmonicity	$2\pi \times 185$ MHz
T_B^1	detector qubit lifetime ($\Omega_B = 0$)	$5\ \mu\text{s}$
τ_B	detector-state waiting time ($\Omega_B \neq 0$)	$4\ \mu\text{s}$
T_B^2	detector qubit coherence time	$8\ \mu\text{s}$
χ_B	detector qubit-cavity dispersive shift	$2\pi \times 5.1$ MHz
n_B^{th}	detector qubit average thermal population	0.5%
χ_{SB}	system qubit-detector qubit dispersive shift	$2\pi \times 36$ MHz
ω_R	readout cavity resonance frequency	$2\pi \times 8.094$ GHz
κ_R	readout cavity linewidth	$2\pi \times 3.6$ MHz

TABLE S1. System parameters and their respective values, cf. equation (S1). The quoted coherence times are measured in the presence of the readout cavity drive, with the exception of T_B^2 .

A. Drive Configuration

Three microwave drives are applied simultaneously during the experiment (Table S2):

Drive	Description	Frequency	Controlled parameter
Ω_S	system qubit drive	ω_S	Ω_S
Ω_B	detector qubit drive	ω_B	α
Ω_R	readout cavity drive	$\omega_R - \chi_B$	α

TABLE S2. Drives used in this work. The dimensionless measurement strength λ is tuned by varying Ω_B , while Ω_S and Ω_R remain fixed.

The system drive Ω_S induces Rabi oscillations between $|0\rangle$ and $|1\rangle$. The detector drive Ω_B couples $|0\rangle$ to the bright state $|B\rangle$, and the readout drive Ω_R enables continuous monitoring of the $|B\rangle$ population.

To maximise detection fidelity for $|B\rangle$ while minimising decoherence in the system manifold $\{|0\rangle, |1\rangle\}$, we drive the readout at frequency $\omega_R - \chi_B$, which is resonant with the cavity only when the system is in $|B\rangle$. The resulting monitoring rate of the $|B\rangle$ population is [43]

$$\Gamma = \frac{\kappa_R (\chi_B/2)^2 \bar{n}_B}{2(\chi_B/2)^2 + (\kappa_R/2)^2}, \quad (\text{S2})$$

where κ_R is the readout linewidth and $\bar{n}_B \propto |\Omega_R|^2$ is the average intracavity photon number. We extract $\bar{n}_B \approx 12$ using the calibration procedure of ref. [44].

The measurement rate α depends on both Ω_B and Γ . The procedure for extracting α from experimental data is described in the final subsection below.

B. Continuous Monitoring Protocol

The readout signal is integrated over successive intervals of duration T_{int} , producing an integrated voltage value for each interval. These values cluster into two well-separated peaks: “click” (system in $|B\rangle$) and “no-click” (system in $|0\rangle$ or $|1\rangle$). We fit the histogram to a sum of two Gaussians and set the discrimination threshold at their intersection (Fig. S2a,b). To suppress noise-induced misassignments, we apply a Schmitt trigger [45]: any measurement falling within an uncertainty window around the threshold retains the previous state assignment. This produces a binary click record (Fig. S2c).

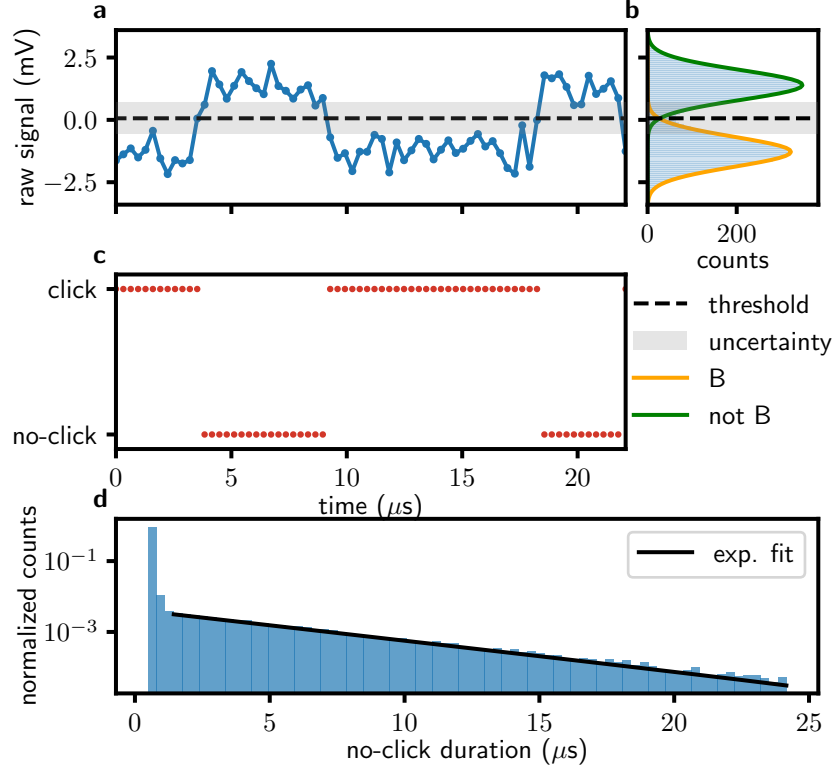


FIG. S2. **Click record extraction.** **a**, Raw integrated measurement signal versus time. **b**, Histogram of measurement outcomes, fitted with a sum of two Gaussians, with typical false-negative/false-positive probabilities of $p_{\text{FP}} = p_{\text{FN}} = 4\%$. The dashed line indicates the discrimination threshold; the grey band marks the uncertainty region used for Schmitt-trigger filtering. **c**, Resulting binary click record. **d**, Distribution of no-click durations with $\Omega_S = 0$, showing exponential decay at rate α (black line). Excess counts in the first few bins (excluded from the fit) arise from false negatives: missed clicks when the system is in $|B\rangle$ produce spurious short-duration no-click intervals.

C. Definition of a Click

In the ideal two-level model setting of ref. [2], a click corresponds to instantaneous projection onto $|0\rangle$. In our three-level system, a click involves three sequential processes: (i) The detector drive Ω_B induces excitations from $|0\rangle$ to $|B\rangle$, (ii) the readout projects the state onto $|B\rangle$, and (iii) the system relaxes back to $|0\rangle$ with relaxation time τ_B . Hence, experimentally, a “click” refers to a measurement outcome indicating detection of the system in $|B\rangle$. The net effect is projection onto $|0\rangle$, as in the ideal model, but with a finite average delay τ_B . The impact of this delay on the dynamics is analysed in Section 5.

D. Extraction of the Measurement Rate α

From the click record, we compute histograms of no-click durations — the time the system remains within the $|0\rangle-|1\rangle$ manifold before a click occurs. With the system drive off ($\Omega_S = 0$) and the system initialised in $|0\rangle$, these distributions decay exponentially at rate $\alpha(\Omega_B)$, consistent with a Poisson process (Fig. S2d). While fitting this decay provides an initial estimate of α , this approach is sensitive to misassignments. To obtain accurate values, we analyse the click record using a three-state hidden Markov model (HMM) [41] that accounts for misassignments and finite detection fidelity. This HMM is defined by a transition matrix \mathbf{T} and an emission matrix \mathbf{E} . The transition matrix encodes the probabilities p_{ij} of moving from state $|i\rangle$ to state $|j\rangle$ in one time step dt . In our system, transitions occur between $|0\rangle$ and $|B\rangle$ and between $|0\rangle$ and $|1\rangle$, but not directly between $|B\rangle$ and $|1\rangle$. The matrix therefore has the form:

$$\mathbf{T} = \begin{pmatrix} 1 - p_{0B} - p_{01} & p_{0B} & p_{01} \\ p_{B0} & 1 - p_{B0} & 0 \\ p_{10} & 0 & 1 - p_{10} \end{pmatrix}, \quad (\text{S3})$$

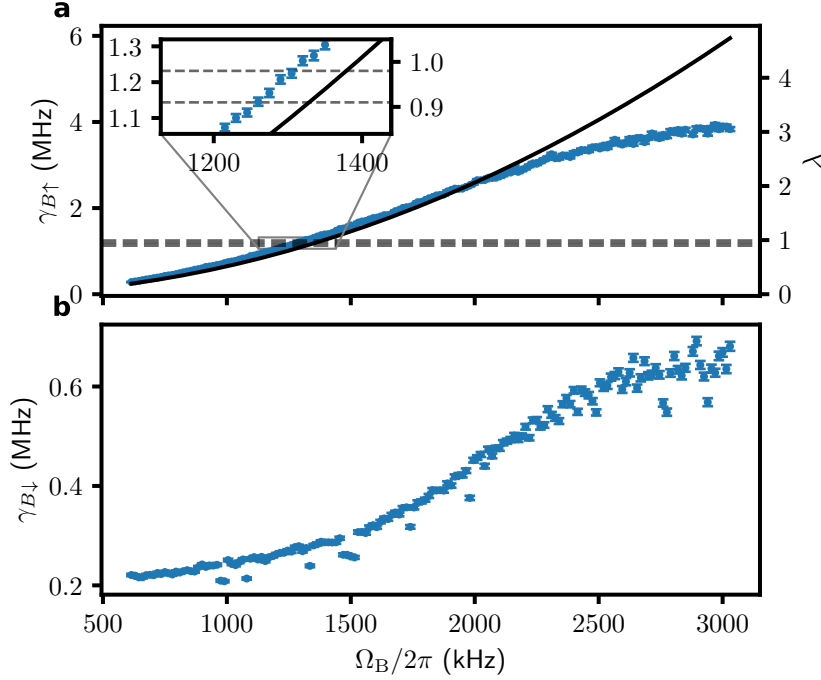


FIG. S3. **Extraction of measurement parameters via HMM analysis.** **a**, Measurement rate $\alpha = \gamma_{B\uparrow}$ versus detector drive amplitude Ω_B . While the measurement rate initially follows the expected quadratic scaling (solid black line), saturation occurs at high drive strengths ($\lambda \gtrsim 2$). Dashed grey lines indicate the observed transition values $\lambda_1^{\text{obs}} = 0.99$ and $\lambda_2^{\text{obs}} = 0.92$. Inset: expanded view of the region near the dynamical transitions. **b**, Decay rate $\gamma_{B\downarrow} = \tau_B^{-1}$ versus Ω_B . $\gamma_{B\downarrow}$ is less affected by the drive owing to the Stark shift induced by readout photons. Error bars represent 1σ confidence intervals.

where rows and columns are ordered as $|0\rangle$, $|B\rangle$, $|1\rangle$. These probabilities relate to the underlying rates via

$$(p_{0E}, p_{E0}) = \left(\frac{\gamma_{E\uparrow}}{\Gamma_E} (1 - e^{-\Gamma_E dt}), \frac{\gamma_{E\downarrow}}{\Gamma_E} (1 - e^{-\Gamma_E dt}) \right), \quad \Gamma_E = \gamma_{E\uparrow} + \gamma_{E\downarrow},$$

for $E \in \{B, 1\}$, where $\gamma_{E\uparrow}$ and $\gamma_{E\downarrow}$ are the excitation and relaxation rates between $|0\rangle$ and $|E\rangle$. These relate to the parameters used elsewhere in this paper as follows: the measurement rate is $\alpha = \gamma_{B\uparrow}$, the inverse waiting time in $|B\rangle$ is $\tau_B^{-1} = \gamma_{B\downarrow}$, and the qubit relaxation rate is $(T_S^1)^{-1} = \gamma_{1\downarrow}$.

The emission matrix encodes the probability of observing each outcome (click or no-click) given the hidden state. Only $|B\rangle$ should produce clicks, while $|0\rangle$ and $|1\rangle$ should both yield no-click outcomes. Detection errors modify these ideal probabilities: a false positive (probability p_{FP}) registers a click when the system is not in $|B\rangle$, while a false negative (probability p_{FN}) misses a click when the system is in $|B\rangle$. The emission matrix is therefore

$$\mathbf{E} = \begin{pmatrix} 1 - p_{\text{FP}} & p_{\text{FP}} \\ p_{\text{FN}} & 1 - p_{\text{FN}} \\ 1 - p_{\text{FP}} & p_{\text{FP}} \end{pmatrix}, \quad (\text{S4})$$

with columns ordered as no-click, click. The identical first and third rows reflect that $|0\rangle$ and $|1\rangle$ are indistinguishable to the detector.

We use the Baum-Welch algorithm [41] to find the parameters that maximise the likelihood of the observed click record. Initial guesses for $\gamma_{1\uparrow}$ and $\gamma_{1\downarrow}$ come from independent T_1 and thermal population measurements, those for $\gamma_{B\uparrow}$ and $\gamma_{B\downarrow}$ from exponential fits to click/no-click intervals, and those for p_{FP} and p_{FN} from the Gaussian separation in the readout histogram. From the optimised transition matrix, we extract α and τ_B , which are used in all numerical simulations (Supplementary Information Sections 5 and 8).

Figure S3 shows the extracted rates versus detector drive amplitude Ω_B . The measurement rate α increases approximately quadratically with Ω_B , consistent with the expected scaling $\alpha \propto \Omega_B^2/\Gamma$. In contrast, the waiting time τ_B varies less across the range of drive amplitudes. This is because the readout photons induce a Stark shift that detunes the detector qubit transition once the system reaches $|B\rangle$. Instead, τ_B is determined primarily by the intrinsic

lifetime of the detector qubit $T_B^1 \approx 5 \mu s$. In the range of Ω_B where the dynamical transitions occur, we find $\tau_B \approx 4 \mu s$ (Supplementary Table S1).

SI 4: Overview of the Ideal Model of Monitored Qubit Dynamics

In this section, we review the ideal model of monitored qubit dynamics as presented in ref. [2], adapting the notation and derivation for clarity.

A. No-Click Dynamics of a Monitored Qubit

We consider a coherently driven qubit with Hamiltonian

$$\hat{H}_d/\hbar = \frac{\Omega_S}{2} \hat{\sigma}_y. \quad (\text{S5})$$

The qubit ground state $|0\rangle$ is monitored by a sequence of partial measurements performed at intervals $dt \ll \Omega_S^{-1}$. Each measurement yields either a *click* or *no-click* outcome—associated with the Kraus operators

$$\hat{M}_{\text{click}} = \sqrt{p} |0\rangle\langle 0|, \quad \hat{M}_{\text{no-click}} = |1\rangle\langle 1| + \sqrt{1-p} |0\rangle\langle 0|, \quad (\text{S6})$$

with $p \in [0, 1]$ the per-interval measurement strength. In the limit $dt \rightarrow 0$, we keep the effective measurement rate $\alpha \equiv \frac{p}{dt}$ fixed, so that $p = \alpha dt \ll 1$ per time step. The dimensionless measurement strength is then $\lambda = \alpha/(2\Omega_S)$.

Expanding $\hat{M}_{\text{no-click}}$ to first order in p and combining with the unitary evolution $\hat{U} \approx \mathbb{I} - i\frac{\Omega_S}{2} \hat{\sigma}_y dt$, the no-click evolution takes the form $\hat{M}_{\text{no-click}} \hat{U} \approx \mathbb{I} - \frac{i}{\hbar} \hat{H}_{\text{eff}} dt$, yielding the effective non-Hermitian Hamiltonian of equation (1):

$$\hat{H}_{\text{eff}}/\hbar = \frac{\Omega_S}{2} (\hat{\sigma}_y - 2i\lambda |0\rangle\langle 0|). \quad (\text{S7})$$

Since the dynamics are constrained to the XZ -plane, the qubit state is fully characterised by the polar angle $\theta(t)$ of its Bloch vector $|\psi[\theta(t)]\rangle = \cos\left(\frac{\theta(t)}{2}\right) |1\rangle + \sin\left(\frac{\theta(t)}{2}\right) |0\rangle$. Note that $\theta = 0$ corresponds to the excited state $|1\rangle$ and $\theta = \pi$ to the ground state $|0\rangle$, opposite to the convention in ref. [2]. The combined evolution leads to the equation of motion:

$$\theta(t + dt) = \begin{cases} \theta(t) - \Omega_S [1 + \lambda \sin \theta(t)] dt & \text{no-click} \\ \pi & \text{click,} \end{cases} \quad (\text{S8})$$

where the click probability per interval is

$$p_{\text{click}}(\theta) = \alpha dt \sin^2\left(\frac{\theta}{2}\right) \equiv r(\theta) dt, \quad (\text{S9})$$

with $r(\theta)$ the instantaneous click rate.

The no-click dynamics depend on λ : for $\lambda < 1$, the angular velocity is always negative, driving $\theta(t)$ anticlockwise around the Bloch sphere. For $\lambda > 1$, two fixed points emerge, $\theta_{\pm} = 2 \arctan(-\lambda \pm \sqrt{\lambda^2 - 1})$, where the angular velocity vanishes. In this regime, the angular velocity is positive for $\theta_- < \theta < \theta_+$, reflecting the competition between the coherent drive and the measurement backaction. Consequently, the range $\theta \in (-\pi, \theta_+)$ constitutes a *forbidden region* inaccessible under no-click evolution. With the initial condition $\theta(0) = \pi$ (i.e., the ground state $|0\rangle$), the solution of equation (S8) is

$$\tan \frac{\theta(t)}{2} = \frac{\sqrt{1 - \lambda^2}}{\tan\left(\frac{1}{2}\Omega_S t \sqrt{1 - \lambda^2}\right)} - \lambda. \quad (\text{S10})$$

For $\lambda < 1$, this describes periodic evolution, while for $\lambda > 1$, the qubit evolves from $\theta = \pi$ at $t = 0$ to $\theta = \theta_+$ at $t = \infty$ — a continuous quantum jump. The transition between these regimes, nominally at $\lambda_1^c = 1$, is visible in Fig. 3a–b.

B. Click Record Statistics

We now turn to the no-click probability $P^{(0)}(t)$, defined as the probability of obtaining no clicks up to time t . Its evolution is governed by

$$\frac{dP^{(0)}(t)}{dt} = -r(\theta(t)) P^{(0)}(t), \quad (\text{S11})$$

where $-dP^{(0)}(t)/dt$ corresponds to the probability density of registering the *first* click at time t , or, equivalently, the distribution of no-click durations.

Combining equation (S9) with the trajectory $\theta(t)$ from equation (S10) yields

$$P^{(0)}(t) = e^{-\lambda\Omega_{\text{st}}t} \frac{-1 + \lambda^2 \cos(\Omega_{\text{st}}t\sqrt{1-\lambda^2}) + \lambda\sqrt{1-\lambda^2} \sin(\Omega_{\text{st}}t\sqrt{1-\lambda^2})}{\lambda^2 - 1}. \quad (\text{S12})$$

Consequently, the distribution of no-click durations is

$$-\frac{dP^{(0)}(t)}{dt} = \lambda\Omega_{\text{st}} e^{-\lambda\Omega_{\text{st}}t} \frac{-1 + (2\lambda^2 - 1) \cos(\Omega_{\text{st}}t\sqrt{1-\lambda^2}) + 2\lambda\sqrt{1-\lambda^2} \sin(\Omega_{\text{st}}t\sqrt{1-\lambda^2})}{\lambda^2 - 1}. \quad (\text{S13})$$

For $\lambda < 1$, the distribution of no-click durations oscillates, matching the periodic no-click dynamics: since $r(\theta) = \alpha \sin^2(\theta/2)$ (equation (S9)), clicks cluster near $\theta = \pi$ and are suppressed near $\theta = 0$. For $\lambda > 1$, the oscillations cease, and the distribution of no-click durations decays exponentially, cf. Fig. 3c. $P^{(0)}(t)$ exhibits the same regimes (oscillating for $\lambda < 1$ and non-oscillating for $\lambda > 1$), making it a suitable observable for identifying the location of the first transition, cf. Fig. S5.

C. Angular Distributions

The second transition is characterised in ref. [2] through the steady-state angular probability density $P_\infty(\theta)$:

$$P_\infty(\theta) = \begin{cases} \frac{\lambda}{(1+\lambda \sin \theta)^2} \left(\frac{\tan \frac{\theta}{2} - \tan \frac{\theta_+}{2}}{\tan \frac{\theta}{2} - \cot \frac{\theta_+}{2}} \right)^{\frac{\lambda}{\sqrt{\lambda^2 - 1}}} & \text{for } \theta \in (\theta_+, \pi] \\ 0 & \text{otherwise.} \end{cases} \quad (\text{S14})$$

This expression diverges at θ_+ for $\lambda > 2/\sqrt{3}$, indicating that the system spends an extended amount of time in the vicinity of θ_+ .

Here, we instead characterise the second transition using the angular dwell-time density $\tau_\theta(\theta)$. Consider a system initialised at $\theta = \pi$. We define the expectation value $\mathbb{E}[T_{\Delta\theta}(\theta)]$ of the time $T_{\Delta\theta}(\theta)$ spent in the interval $[\theta, \theta + \Delta\theta]$ before a click occurs. The dwell-time density is then

$$\tau_\theta(\theta) \equiv \lim_{\Delta\theta \rightarrow 0} \frac{\mathbb{E}[T_{\Delta\theta}(\theta)]}{\Delta\theta}. \quad (\text{S15})$$

Since clicks reset the system to $\theta = \pi$, one expects that $P_\infty(\theta) \propto \tau_\theta(\theta)$. This reflects the fact that the probability density of finding the system state in the vicinity of θ after an infinite evolution duration is proportional to the time the system spends in that vicinity. Equation (S21) below confirms that this is indeed the case.

The expectation value $\mathbb{E}[T_{\Delta\theta}(\theta)]$ can be calculated as follows. For small $\Delta\theta$ and conditioned on the absence of clicks, the time spent in the interval $[\theta, \theta + \Delta\theta]$ is simply the traversal time $T_{\Delta\theta}(\theta) = \Delta\theta/|\dot{\theta}|$, where the angular velocity satisfies $\dot{\theta}(\theta) < 0$, cf. equation (S8). However, when starting from $\theta = \pi$, the system does not always reach this interval: a click may interrupt its trajectory, in which case $T_{\Delta\theta}(\theta) = 0$. The probability of reaching θ is $P^{(0)}(\theta) \equiv P^{(0)}(t(\theta))$, where $t(\theta)$ is the time to reach θ under no-click evolution. Thus, the system spends on average $\mathbb{E}[T_{\Delta\theta}(\theta)] = P^{(0)}(\theta)\Delta\theta/|\dot{\theta}|$ in the interval. Substituting into equation (S15) yields

$$\tau_\theta(\theta) = \frac{P^{(0)}(\theta)}{|\dot{\theta}|}. \quad (\text{S16})$$

The dwell time can also be expressed in terms of the angular first-click density $\rho(\theta)$, defined as the probability density for the first click to occur when the system reaches θ :

$$\rho(\theta) \equiv \frac{dP^{(0)}(\theta)}{d\theta} = -\frac{dP^{(0)}(t)}{dt} \frac{1}{|\dot{\theta}|}. \quad (\text{S17})$$

Using equation (S11), we obtain

$$\rho(\theta) = r(\theta) \frac{P^{(0)}(\theta)}{|\dot{\theta}|}, \quad (\text{S18})$$

which yields

$$\tau_\theta(\theta) = \frac{P^{(0)}(\theta)}{|\dot{\theta}(\theta)|} = \frac{\rho(\theta)}{r(\theta)}. \quad (\text{S19})$$

Combining equations (S17), (S13), (S10), and (S8), we obtain

$$\rho(\theta) = \begin{cases} \frac{2\lambda \sin^2(\frac{\theta}{2})}{(1+\lambda \sin \theta)^2} \left(\frac{\tan \frac{\theta}{2} - \tan \frac{\theta_+}{2}}{\tan \frac{\theta}{2} - \cot \frac{\theta_+}{2}} \right)^{\frac{\lambda}{\sqrt{\lambda^2-1}}} \left(\tan \frac{\theta_+}{2} \right)^{-\frac{2\lambda}{\sqrt{\lambda^2-1}}} & \text{for } \theta \in (\theta_+, \pi] \\ 0 & \text{otherwise.} \end{cases} \quad (\text{S20})$$

Substituting this result into equation (S19) gives

$$\tau_\theta(\theta) = \begin{cases} \frac{1}{\Omega_S(1+\lambda \sin \theta)^2} \left(\frac{\tan \frac{\theta}{2} - \tan \frac{\theta_+}{2}}{\tan \frac{\theta}{2} - \cot \frac{\theta_+}{2}} \right)^{\frac{\lambda}{\sqrt{\lambda^2-1}}} \left(\tan \frac{\theta_+}{2} \right)^{-\frac{2\lambda}{\sqrt{\lambda^2-1}}} & \text{for } \theta \in (\theta_+, \pi] \\ 0 & \text{otherwise.} \end{cases} \quad (\text{S21})$$

In other words, $\tau_\theta(\theta) = (\lambda \Omega_S)^{-1} \left(\tan \frac{\theta_+}{2} \right)^{-\frac{2\lambda}{\sqrt{\lambda^2-1}}} P_\infty(\theta)$.

This expression can be rewritten as

$$\tau_\theta(\theta) = \begin{cases} \frac{1}{\Omega_S} \left(\tan \frac{\theta_+}{2} \right)^{-\frac{2\lambda}{\sqrt{\lambda^2-1}}} \frac{1}{\cos^4 \frac{\theta}{2}} \left(\tan \frac{\theta}{2} - \tan \frac{\theta_+}{2} \right)^{\frac{\lambda}{\sqrt{\lambda^2-1}}-2} \left(\tan \frac{\theta}{2} - \tan \frac{\theta_-}{2} \right)^{-\frac{2\lambda}{\sqrt{\lambda^2-1}}-2} & \text{for } \theta \in (\theta_+, \pi] \\ 0 & \text{otherwise.} \end{cases} \quad (\text{S22})$$

Here we used the relation

$$1 + \lambda \sin \theta = \cos^2 \frac{\theta}{2} \left(\tan \frac{\theta}{2} - \tan \frac{\theta_+}{2} \right) \left(\tan \frac{\theta}{2} - \tan \frac{\theta_-}{2} \right). \quad (\text{S23})$$

The divergence in $\tau_\theta(\theta)$ thus arises when the critical exponent $\xi(\lambda) \equiv (\lambda/\sqrt{\lambda^2-1})-2$ crosses 0, i.e., at $\lambda = \lambda_2^c = 2/\sqrt{3}$.

When initialising the system at $\theta = 0$ (as in the main text), rather than at $\theta = \pi$ (as above), there are two differences: (i) the system does not visit $\theta > 0$ before a click occurs; (ii) $\tau_\theta(\theta)$ is multiplied by a constant factor because in the new setting $P^{(0)}(\theta = 0) = 1$ (as opposed to $P^{(0)}(\theta = \pi) = 1$). This ultimately yields formula (4) used to fit the experimental data curves $\tau_\theta(\lambda, \theta)$ close to the fixed point θ_+ , and to identify the observed transition as $\lambda_2^{\text{obs}} \equiv \lambda(\xi = 0)$ (Fig. 4 and Methods).

SI 5: Realistic Model of Monitored Qubit Dynamics

In this section, we extend the ideal model of Supplementary Information Section 4 and ref. [2] to account for realistic experimental conditions:

- Pure dephasing, modelled as Markovian fluctuations of the relative phase between $|0\rangle$ and $|1\rangle$, quantified by the pure dephasing time T_S^ϕ . This dephasing is primarily induced by the readout cavity drive.
- Relaxation, describing spontaneous decay from $|1\rangle$ to $|0\rangle$ with lifetime T_S^1 ;

- Detector inefficiency, manifesting as false positives (spurious clicks at rate $\kappa_{\text{FP}} \equiv p_{\text{FP}}/dt$, cf. Supplementary Information Section 3 D) and false negatives (true clicks missed with probability p_{FN});
- Finite waiting time τ_B in the detector qubit's excited state $|B\rangle$ (cf. Fig. S3): after a click, the system is projected onto $|B\rangle$ and remains there before relaxing back to $|0\rangle$;
- Finite integration time T_{int} , arising because the detection signal is integrated over a nonzero window, reducing temporal resolution compared to the idealised instantaneous measurements.

Dephasing, relaxation, detector inefficiency, and finite waiting time admit analytical treatment, developed below. Finite integration time is incorporated into the numerical simulations (Section 8).

A. Dephasing and Relaxation

The pure-state dynamics of Section 4 assumed ideal measurements and no decoherence. To incorporate dephasing and relaxation, we use the density matrix formalism.

a. Ensemble dynamics. The unconditional evolution is governed by the Lindblad master equation (2), extended to include dephasing and relaxation:

$$\frac{d\rho}{dt} = \mathcal{L}[\rho] = -\frac{i}{\hbar}[\hat{H}_d, \rho] + \alpha \mathcal{D}[|0\rangle\langle 0|]\rho + \frac{1}{2T_S^\phi} \mathcal{D}[\sigma_z]\rho + \frac{1}{T_S^1} \mathcal{D}[|0\rangle\langle 1|]\rho, \quad (\text{S24})$$

where $\mathcal{D}[\hat{L}]\rho = \hat{L}\rho\hat{L}^\dagger - \frac{1}{2}\{\hat{L}^\dagger\hat{L}, \rho\}$ is the standard dissipator. The three dissipative terms describe the measurement backaction, dephasing, and relaxation, respectively.

b. Postselected dynamics. For evolution conditioned on no clicks, the quantum-jump term $\hat{L}\rho\hat{L}^\dagger$ of the measurement dissipator is removed, yielding the postselected Liouvillian \mathcal{L}_P :

$$\frac{d\rho}{dt} = \mathcal{L}_P[\rho] = -\frac{i}{\hbar}[\hat{H}_d, \rho] - \frac{\alpha}{2}\{|0\rangle\langle 0|, \rho\} + \frac{1}{2T_S^\phi} \mathcal{D}[\sigma_z]\rho + \frac{1}{T_S^1} \mathcal{D}[|0\rangle\langle 1|]\rho. \quad (\text{S25})$$

This evolution is not trace-preserving: $\text{Tr}[\rho(t)]$ gives the no-click probability $P^{(0)}(t)$. In the absence of decoherence, equation (S25) reduces to the pure-state no-click dynamics of Section 4.

B. Detector Inefficiency

In practice, the measurement record is affected by detection errors: false positives (a click is registered when none occurred) and false negatives (a true click goes undetected). False positives occur spontaneously at rate κ_{FP} , independent of the system state. False negatives occur with probability p_{FN} whenever a true click happens.

a. Ensemble dynamics. The unconditional evolution is unaffected by detector inefficiency: the true measurement backaction occurs regardless of whether the detector correctly reports it. The ensemble Liouvillian remains equation (S24).

b. Postselected dynamics. For evolution conditioned on no *registered* clicks, detector errors modify the dynamics in two ways.

First, consider false positives. A postselected trajectory ends when a click is registered, which can happen either due to a true click or a false positive. In the ideal case, the no-click probability decreases at a rate $\alpha|0\rangle\langle 0|$ due to true clicks, captured by the anticommutator $-\frac{\alpha}{2}\{|0\rangle\langle 0|, \rho\}$. False positives provide an additional, state-independent channel for trajectory termination, contributing a uniform decay $-\kappa_{\text{FP}}\rho$.

Second, consider false negatives. When a true click occurs but goes undetected, the system experiences the measurement backaction—projection onto $|0\rangle$ —yet the trajectory continues since no click was registered. In the ideal postselected dynamics, the quantum-jump term $\alpha|0\rangle\langle 0|\rho|0\rangle\langle 0|$ is absent because clicks terminate the trajectory. With false negatives, a fraction p_{FN} of clicks go undetected, so this term is partially restored: $p_{\text{FN}}\alpha|0\rangle\langle 0|\rho|0\rangle\langle 0|$.

Combining these effects, the postselected Liouvillian becomes

$$\tilde{\mathcal{L}}_P[\rho] = -\frac{i}{\hbar}[\hat{H}_d, \rho] - \frac{\alpha}{2}\{|0\rangle\langle 0|, \rho\} - \kappa_{\text{FP}}\rho + p_{\text{FN}}\alpha|0\rangle\langle 0|\rho|0\rangle\langle 0| + \frac{1}{2T_S^\phi} \mathcal{D}[\sigma_z]\rho + \frac{1}{T_S^1} \mathcal{D}[|0\rangle\langle 1|]\rho. \quad (\text{S26})$$

The eigenvalue structure of $\tilde{\mathcal{L}}_P$ determines the first two transition points, as analysed in Section 6.

C. Finite waiting time in $|B\rangle$

When a click occurs, the system is projected onto $|B\rangle$ and returns to the qubit subspace only after a finite waiting time τ_B . Since postselected trajectories condition on no clicks, the system never reaches $|B\rangle$ and the waiting time does not affect the postselected dynamics. However, it does modify the ensemble dynamics:

$$\begin{aligned}\partial_t \rho_S(t) &= \mathcal{L}_P[\rho_S] + \frac{p_B}{\tau_B} |0\rangle\langle 0|, \\ \partial_t p_B(t) &= \alpha \langle 0| \rho_S |0\rangle - \frac{p_B}{\tau_B},\end{aligned}\quad (\text{S27})$$

where ρ_S is the density matrix in the qubit subspace and p_B is the population in $|B\rangle$. Since the ensemble dynamics are not influenced by detection errors, this expression uses \mathcal{L}_P rather than $\tilde{\mathcal{L}}_P$. In the limit $\tau_B \rightarrow \infty$, the system never returns from $|B\rangle$, and the qubit dynamics reduce to the postselected evolution. In the opposite limit $\tau_B \rightarrow 0$, the population returns instantaneously: setting $\partial_t p_B = 0$ gives $p_B/\tau_B = \alpha \langle 0| \rho_S |0\rangle$, and substituting into the first equation recovers the ensemble dynamics of equation (S24).

SI 6: The Transition Locations in the Realistic Model

We analyse how decoherence modifies the locations of the dynamical transitions, building on the realistic model of Section 5. Since the eigenvalue structure of the relevant Liouvillians fully determines the transitions, we compute the critical measurement strengths numerically by exact diagonalisation.

A. Postselected Liouvillian with Decoherence

The first two transitions are determined by the no-click dynamics, governed by the postselected Liouvillian $\tilde{\mathcal{L}}_P$ of equation (S26). To analyse its eigenvalue structure, we parametrise the density matrix in the $|1\rangle-|0\rangle$ basis as

$$\rho_S(t) = \frac{1}{2} \begin{pmatrix} p_S + z & x \\ x & p_S - z \end{pmatrix}, \quad (\text{S28})$$

where $p_S = \text{Tr}[\rho_S]$ is the no-click probability, $z = \langle \sigma_z \rangle$, and $x = \langle \sigma_x \rangle$. The coherence x is real since the dynamics preserve the XZ -plane of the Bloch sphere.

Converting equation (S26) to the vector representation $\mathbf{s} = [p_S, x, z]^T$ yields

$$\frac{d\mathbf{s}}{dt} = \tilde{\mathcal{L}}_P \mathbf{s}, \quad (\text{S29})$$

with matrix representation

$$\tilde{\mathcal{L}}_P = \begin{pmatrix} -\frac{\alpha_{\text{eff}}}{2} - \kappa_{\text{FP}} & 0 & \frac{\alpha_{\text{eff}}}{2} \\ 0 & -\gamma_2 - \frac{\alpha}{2} - \kappa_{\text{FP}} & \Omega_S \\ \frac{\alpha_{\text{eff}}}{2} - \gamma_1 & -\Omega_S & -\frac{\alpha_{\text{eff}}}{2} - \gamma_1 - \kappa_{\text{FP}} \end{pmatrix}. \quad (\text{S30})$$

Here, $\alpha_{\text{eff}} = \alpha(1 - p_{\text{FN}})$ is the effective click rate, $\gamma_1 = 1/T_S^1$ is the relaxation rate, and $\gamma_2 = 1/T_S^\phi + 1/(2T_S^1)$ is the total decoherence rate (including the contribution from relaxation).

The eigenvalues of $\tilde{\mathcal{L}}_P$ determine the transition locations. We order them by their real parts: $\text{Re}(e_1) \leq \text{Re}(e_2) \leq e_3 < 0$, where e_3 is always real while e_1 and e_2 form a complex conjugate pair in the oscillatory regime.

B. The First Transition: Cessation of Oscillations

The first transition marks the boundary between oscillatory and non-oscillatory no-click dynamics. It occurs when e_1 and e_2 transition from complex conjugates to distinct real values, passing through a degenerate point. This requires the characteristic polynomial $\mathcal{C}_P(\Lambda) = \det(\tilde{\mathcal{L}}_P - \Lambda \mathbb{I})$ to have a repeated root, i.e., $\mathcal{C}_P(\Lambda) = 0$ and $\mathcal{C}'_P(\Lambda) = 0$ simultaneously.

In the ideal case, the transition occurs at $\lambda_1^c = 1$. With finite decoherence, the critical point shifts. We determine λ_1^c by numerically finding where the discriminant of $\mathcal{C}_P(\Lambda)$ vanishes. As shown in Fig. S4, λ_1^c rises with increasing decoherence. For our experimental parameters ($T_S^1 = 93 \mu\text{s}$, $T_S^\phi = 26 \mu\text{s}$, $\Omega_S/2\pi = 100 \text{ kHz}$), numerical diagonalisation yields $\lambda_1^c \approx 1.18$. Note that in our setup, the finite waiting time in $|\text{B}\rangle$ allows for repeated integration windows, resulting in a negligibly small probability of not registering a click, i.e., effectively $p_{\text{FN}} \approx 0$. The false positive rate κ_{FP} does not affect λ_1^c because false positives are state-independent and thus cannot influence the dynamics governing the transition.

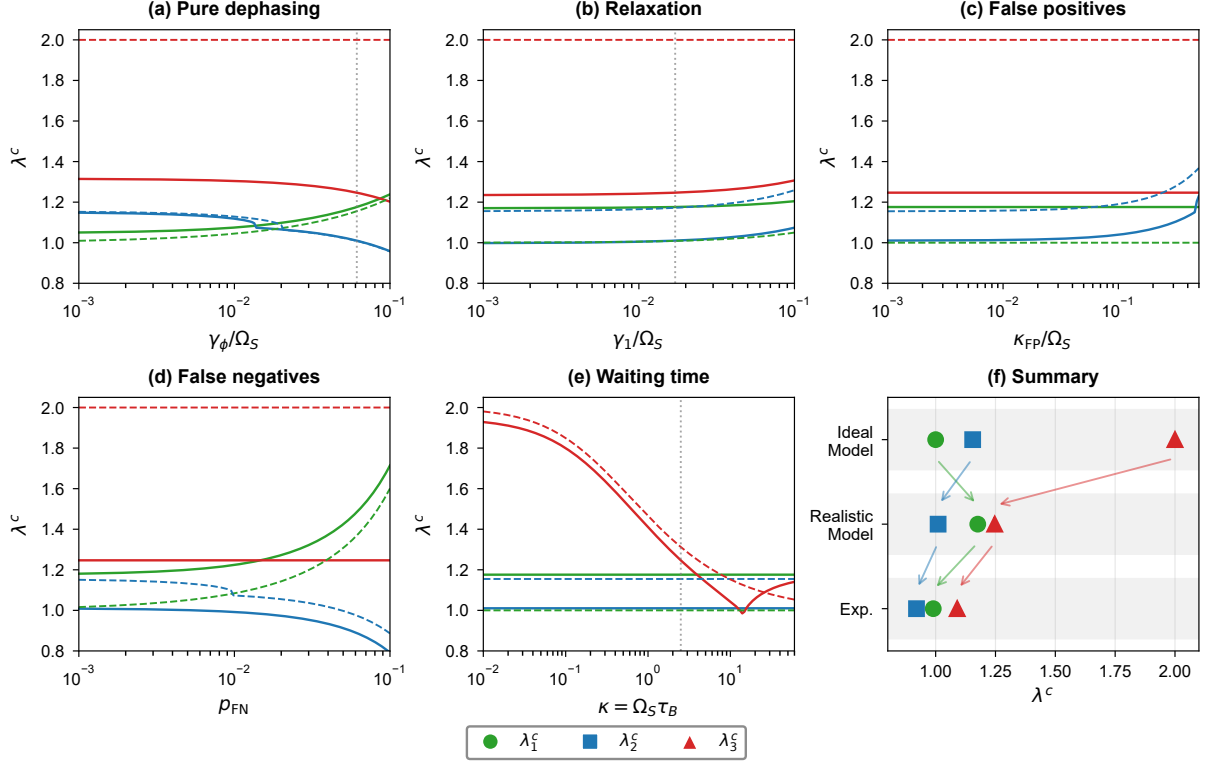


FIG. S4. **Dependence of transition locations on decoherence parameters.** Dashed lines show numerical results from the realistic model with the indicated parameter varied and all others set to zero; solid lines show results with all other parameters held at experimental values. The first, second, and third transition locations are shown in green, blue, and red, respectively. Vertical dotted lines indicate experimental parameter values. (a) Effect of pure dephasing rate γ_ϕ/Ω_S , with $\gamma_\phi = 1/T_S^\phi$. (b) Effect of relaxation rate γ_1/Ω_S . (c) Effect of false positive rate $\kappa_{\text{FP}}/\Omega_S$. (d) Effect of false negative probability p_{FN} . (e) Effect of dimensionless waiting time $\kappa = \Omega_S \tau_B$. (f) Summary comparing ideal values ($\lambda_1^c = 1$, $\lambda_2^c = 2/\sqrt{3}$, $\lambda_3^c = 2$), realistic model predictions ($\lambda_1^c = 1.18$, $\lambda_2^c = 1.01$, $\lambda_3^c = 1.25$), and experimental values ($\lambda_1^{\text{obs}} = 0.99$, $\lambda_2^{\text{obs}} = 0.92$, $\lambda_3^{\text{obs}} = 1.09$). The inverted ordering $\lambda_2^c < \lambda_1^c$ is reproduced by the realistic model and confirmed experimentally.

C. The Second Transition: Onset of State Freezing

The second transition marks the onset of state freezing near the fixed point θ_+ . The transition arises from the competition between two rates: the click rate at the fixed point $-e_3$ and the approach rate to the fixed point $-\text{Re}(e_2) + e_3$. As a result of this competition, the dwell time near the fixed point scales as $\tau_\theta(\theta) \sim |\theta - \theta_+|^\xi$, where the critical exponent is

$$\xi = \frac{e_3}{\text{Re}(e_2) - e_3} - 1 = \frac{2e_3 - \text{Re}(e_2)}{\text{Re}(e_2) - e_3}. \quad (\text{S31})$$

The transition occurs when $\xi = 0$, i.e., when $\text{Re}(e_2) = 2e_3$.

In the ideal model, all eigenvalues are real for $\lambda > 1$:

$$e_3 = -\Omega_S(\lambda - \sqrt{\lambda^2 - 1}), \quad e_2 = -\lambda\Omega_S, \quad e_1 = -\Omega_S(\lambda + \sqrt{\lambda^2 - 1}), \quad (\text{S32})$$

and the condition $e_2 = 2e_3$ yields $\lambda_2^c = 2/\sqrt{3} \approx 1.155$. With finite decoherence, however, the transition location shifts (Fig. S4). Notably, dephasing *lowers* the location of the second transition, in contrast to its effect on the first transition. Moreover, false positives do impact the second transition, increasing λ_2^c . However, in our experiment, Schmitt-trigger filtering (Supplementary Information Section 3) strongly suppresses the effective false-positive rate, well below its raw value $\kappa_{\text{FP}} \equiv p_{\text{FP}}/dt \approx 125 \text{ ms}^{-1}$. Therefore, we set $\kappa_{\text{FP}} = 0$ in the realistic model. For our experimental parameters, numerical analysis yields $\lambda_2^c \approx 1.01$, confirming that dephasing can invert the ordering of the first two transitions.

D. The Third Transition: Onset of Quantum Zeno Dynamics

The third transition occurs in the ensemble dynamics, marking the boundary between oscillatory and overdamped relaxation to the steady state. Unlike the first two transitions, it is primarily affected by the finite waiting time τ_B in the detector's excited state.

The ensemble dynamics including the detector's excited state are given by equation (S27). Extending the parametrisation (S28) to include the detector population, we define $\mathbf{v} = [p_B, p_S, x, z]^T$. The evolution becomes $d\mathbf{v}/dt = \mathcal{L}_B \mathbf{v}$, with

$$\mathcal{L}_B = \begin{pmatrix} -\frac{1}{\tau_B} & \frac{\alpha}{2} & 0 & -\frac{\alpha}{2} \\ \frac{1}{\tau_B} & -\frac{\alpha}{2} & 0 & \frac{\alpha}{2} \\ 0 & 0 & -\gamma_2 - \frac{\alpha}{2} & \Omega_S \\ -\frac{1}{\tau_B} & \frac{\alpha}{2} - \gamma_1 & -\Omega_S & -\frac{\alpha}{2} - \gamma_1 \end{pmatrix}. \quad (\text{S33})$$

Note that the ensemble dynamics are independent of detector inefficiency, since the physical measurement backaction occurs regardless of detection outcome.

The third transition occurs when the characteristic polynomial $\mathcal{C}_B(\Lambda) = \det(\mathcal{L}_B - \Lambda \mathbb{I})$ has a repeated root. The waiting time τ_B interpolates between two limits: for $\tau_B \rightarrow 0$, the system returns instantly from $|B\rangle$ to $|0\rangle$, recovering the standard ensemble dynamics with $\lambda_3^c = 2$ in the ideal case. For $\tau_B \rightarrow \infty$, the system never returns, and the ensemble dynamics reduce to the postselected dynamics, giving $\lambda_3^c \rightarrow \lambda_1^c$. As shown in Fig. S4(e), λ_3^c drops significantly even for modest τ_B : for $\kappa \equiv \Omega_S \tau_B = 2.5$ (our experimental value), numerical diagonalisation gives $\lambda_3^c \approx 1.25$.

SI 7: Extraction of Observed Transition Values

In this section, we detail the procedures used to extract the observed transition locations $\{\lambda_i^{\text{obs}}\}$ from the raw trajectories and derived observables, expanding on the overview in the Methods section.

A. First transition — λ_1^{obs}

The matrix in equation (S30) has three eigenvalues and therefore predicts that, even in the presence of decoherence, the dynamics of $P^{(0)}(t)$ — the probability that no detector clicks have occurred up to time t — are described by a linear combination of three complex exponentials. The first transition is the point where two of these eigenvalues coalesce. In the Laplace domain, the eigenvalues correspond to poles; away from the transition the pole set comprises a complex-conjugate pair e_1, e_2 and a real pole; at the transition the pair becomes real, leaving only real poles and hence purely decaying dynamics.

We extract the three poles of $P^{(0)}(t)$ using the matrix pencil method [42], a high-resolution technique for estimating the poles of complex exponentials, setting the model order to three. Confidence intervals are estimated with a residual bootstrap procedure separately for each λ . First, a fitted curve is constructed from the poles and amplitudes of the complex exponentials obtained with the matrix pencil method. Then, residuals are calculated by subtracting the fit from the experimental $P^{(0)}(t)$ data. In each of the 2000 bootstrap iterations, synthetic data are generated by sampling these residuals with replacement and adding them to the fitted curve. The matrix pencil method is then reapplied to the synthetic data. Consistent tracking of the pole labelling across different bootstrap iterations is enforced by a fixed sorting convention. Finally, we record the median and 1σ confidence interval for both the real and imaginary components of each pole, see Fig. S5.

At the critical measurement strength λ_1^{obs} , two eigenvalues coalesce, and the Liouvillian in equation (S30) acquires a Jordan block structure. Expanding around this transition, the eigenvalue splitting depends on the perturbation

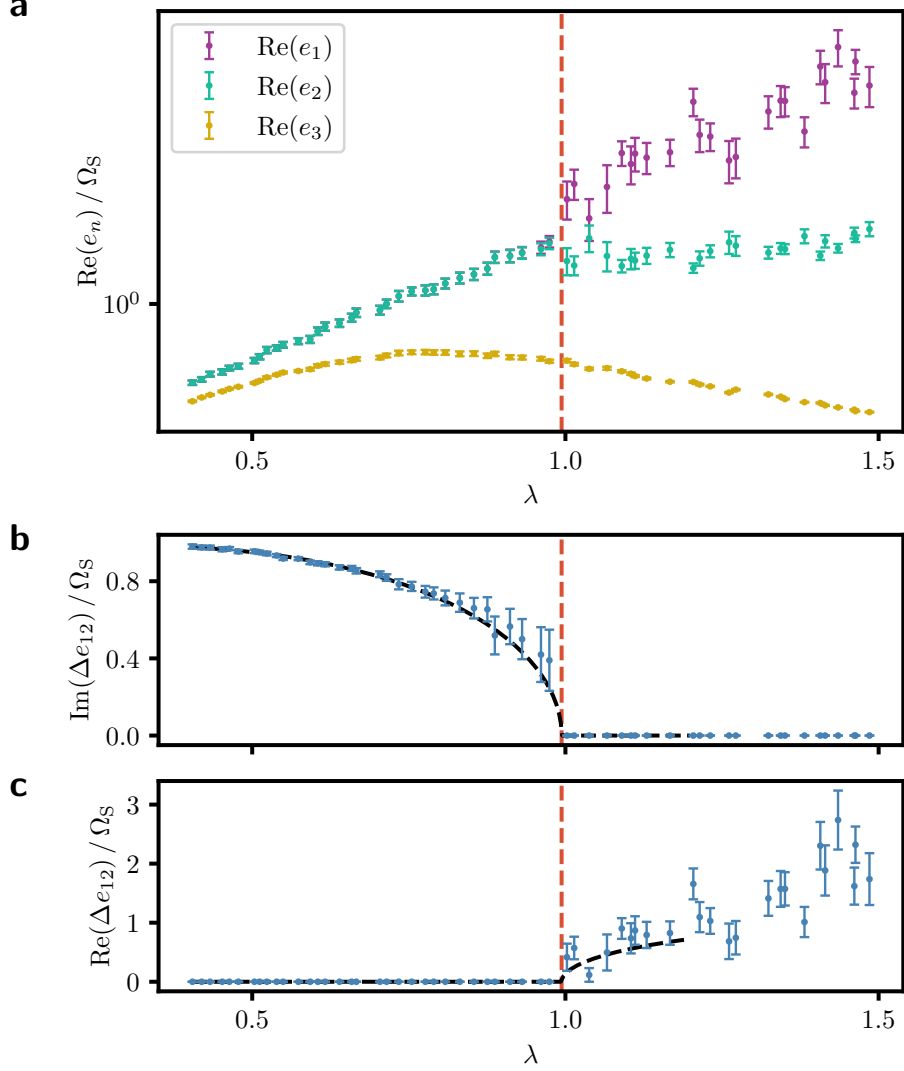


FIG. S5. Extracting λ_1^{obs} from the pole spectrum of the no-click probability $P^{(0)}(t)$. **a**, Real parts of the three poles governing $P^{(0)}(t)$; **b**, **c**, imaginary and real components of the pole splitting $\Delta e_{12} = (e_1 - e_2)/2$, all obtained from the matrix pencil method. Points show the bootstrap median and error bars indicate a 1σ -equivalent uncertainty. The transition is characterised by the vanishing of the imaginary component and the emergence of a real component. The dashed black line shows a joint fit of the real and imaginary parts to equation (3) near the critical point. The vertical red line marks the location of the first transition, measured to be $\lambda_1^{\text{obs}} = 0.99 \pm 0.01$.

$\delta = \lambda - \lambda_1^{\text{obs}}$. While the individual eigenvalues also experience common-mode shifts, these cancel out when taking the difference between them. Consequently, the splitting itself is governed by the expansion of the discriminant of the characteristic polynomial, $\sqrt{\alpha\delta + \beta\delta^2 + \dots}$. Taylor expanding this term yields an expansion of half-integer powers: $\delta^{1/2}, \delta^{3/2}, \dots$ [46], justifying the form of equation (3), which captures the critical point and the behaviour up to second order.

By treating the two components $\text{Re}(\Delta e_{12})$ and $\text{Im}(\Delta e_{12})$ as a combined data set, we fit them simultaneously to equation (3) with a single shared parameter set. Since the expansion holds locally, the fit only uses a narrow window around the initial guess for λ_1^{obs} . Varying the size of this window over a reasonable range leaves λ_1^{obs} unchanged within uncertainties, yielding $\lambda_1^{\text{obs}} = 0.99 \pm 0.01$.

Benchmarking this extraction procedure on simulations of $P^{(0)}(t)$ including shot noise indicates a systematic underestimate of the extracted λ_1^{obs} by ≈ 0.1 . This bias may partially account for the discrepancy between the realistic model (Supplementary Information Section 5) and the observed value.

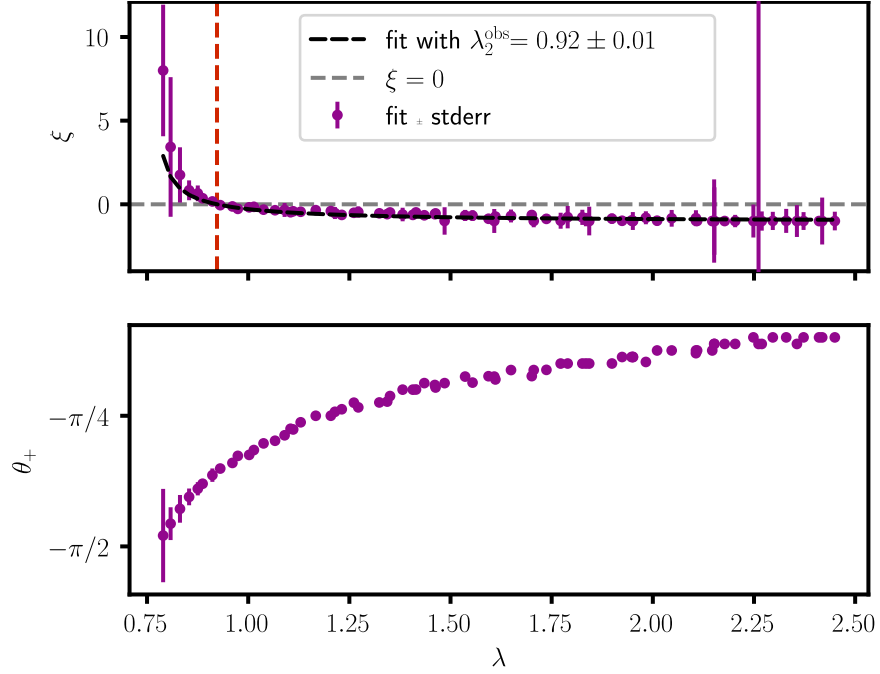


FIG. S6. **Extraction of λ_2^{obs} from the fitted critical exponent ξ .** This figure complements Fig. 4 by showing the fitted values of ξ obtained from the angular dwell-time data $\tau_\theta(\theta)$. Each $\tau_\theta(\theta)$ trace is fitted near its first non-vanishing bin ($\approx \theta_+$) to the analytical model described in Methods, yielding the parameters ξ (top), θ_+ (bottom), and a scaling factor A (not shown). The dashed black line shows the fit of $\xi(\lambda)$ to the analytical model. The second transition is identified from this fit at $\lambda_2^{\text{obs}} = 0.92 \pm 0.01$ (dashed red vertical line), corresponding to the zero crossing $\xi(\lambda_2^{\text{obs}}) = 0$ (horizontal grey dashed line), where the dwell time transitions from finite to divergent.

B. Second transition — λ_2^{obs}

The second transition, which concerns the divergence of the dwell time $\tau_\theta(\theta; \lambda) \sim |\theta - \theta_+|^{\xi(\lambda)}$ near the fixed point θ_+ , is identified from the zero crossing of the critical exponent $\xi(\lambda_2^{\text{obs}}) = 0$. Within the accessible sector $\theta_+ \leq \theta \leq 0$, the expression for the dwell time is (section 4)

$$\tau_\theta(\theta | A, \theta_+, \xi) = \frac{A}{\cos^4(\frac{\theta}{2})} \frac{(\tan \frac{\theta}{2} - \tan \frac{\theta_+}{2})^\xi}{(\tan \frac{\theta}{2} - \cot \frac{\theta_+}{2})^{\xi+4}}, \quad \tau_\theta = 0 \text{ for } \theta < \theta_+, \quad (\text{S34})$$

where we treat (A, θ_+, ξ) as free parameters. We fit the experimental dwell-time data for each λ around an initially guessed θ_+ to the bin-averaged model of equation S34:

$$\tau_{\text{bin}}(\theta_n^{\text{center}}) = \frac{1}{\Delta\theta} \int_{\theta_n}^{\theta_{n+1}} \tau_\theta(\vartheta | A, \theta_+, \xi) d\vartheta, \quad \theta_n^{\text{center}} = \frac{1}{2}(\theta_n + \theta_{n+1}).$$

We then fit the extracted $\xi(\lambda)$ to equation 5, allowing a horizontal shift $\delta\lambda$:

$$\xi_{\text{fit}} = \frac{\lambda - \delta\lambda}{\sqrt{(\lambda - \delta\lambda)^2 - 1}} - 2, \quad (\text{S35})$$

yielding $\lambda_2^{\text{obs}} = 0.92 \pm 0.01$ as the zero-crossing location of ξ_{fit} , with the uncertainty being the 1σ confidence interval.

Using equation (S31), the second transition can be independently inferred from the pole analysis of the no-click probability $P^{(0)}(t)$ (Fig. S5), yielding a consistent result.

C. Third transition — λ_3^{obs}

The third transition is extracted from the spectral analysis of the ensemble-averaged excited state probability $P_{|1\rangle}^{\text{ens}}$, modelled by the Liouvillian in equation (S33). Although the full spectrum contains four eigenvalues, for our

experimental parameters one real eigenvalue is large and negative. The corresponding eigenmode decays too rapidly to be resolved, given the experimental time resolution T_{int} , rendering it effectively unobservable. Furthermore, one eigenvalue is strictly zero, representing a steady-state solution. The remaining two eigenvalues form a complex-conjugate pair. This effective three-pole structure is confirmed by the singular value decomposition (SVD) step of the matrix pencil method [42], which reveals a rank three model — a zero pole and a complex-conjugate pair. We extract all three poles and track the two oscillatory poles, e_1 and e_2 . Analogous to the analysis of λ_1^{obs} , we identify the transition at the coalescence point of this pair. We jointly fit both components of their difference $\text{Re}(\Delta e_{12})$ and $\text{Im}(\Delta e_{12})$ to the near-transition form of equation (3) with a shared fitting parameter set, yielding $\lambda_3^{\text{obs}} = 1.09 \pm 0.01$ (Fig. S7).

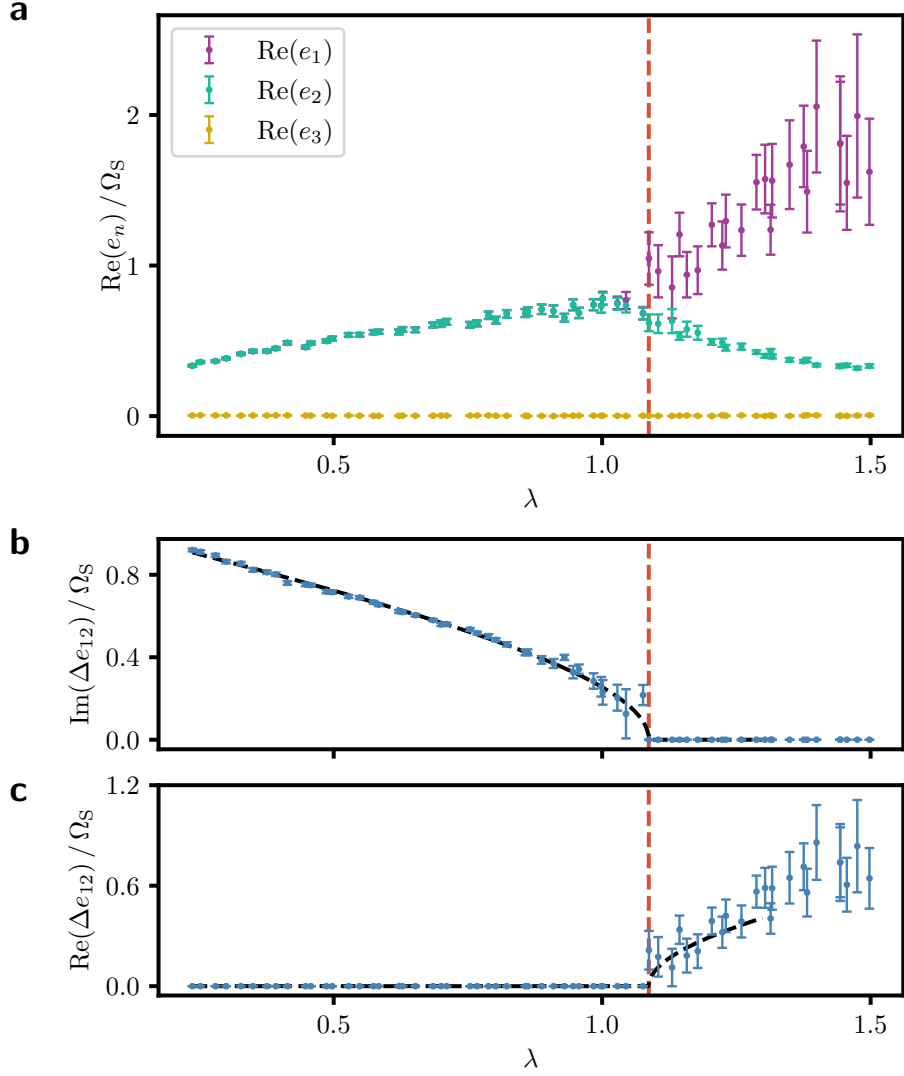


FIG. S7. **Extracting λ_3^{obs} from the pole spectrum of the ensemble-averaged excited state probability $P_{|1\rangle}^{\text{ens}}$.** **a**, Real parts of the three poles governing the dynamics of $P_{|1\rangle}^{\text{ens}}$; **b, c**, imaginary and real components of the pole splitting $\Delta e_{12} = (e_1 - e_2)/2$. Points show the bootstrap median and error bars indicate a 1σ -equivalent uncertainty. As in the first transition, the critical point is identified by the simultaneous vanishing of the imaginary component and the emergence of a real component. The dashed black line shows a joint fit of the real and imaginary parts to equation (3). The vertical red line marks the location of the third transition, measured at $\lambda_3^{\text{obs}} = 1.09 \pm 0.01$.

Similar to the first transition, the extraction procedure may underestimate λ_3^{obs} , potentially accounting in part for the discrepancy with the prediction from the realistic model (Supplementary Information Section 5).

SI 8: Numerical Simulations and Error Budget

We validate our experimental results using Monte Carlo trajectory simulations with independently measured system parameters. Each trajectory is evolved in time steps of $dt_{\text{sim}} = 10 \text{ ns}$. Within each time step, the qubit undergoes unitary evolution governed by equation (S8) followed by stochastic collapse events that include dephasing, relaxation, thermal excitation, and measurement-induced transitions from $|0\rangle$ to $|B\rangle$.

To emulate the experimental detection process, we group the simulation into intervals of duration T_{int} (corresponding to $\frac{T_{\text{int}}}{dt_{\text{sim}}}$ time steps) and compute the total time T_B spent in $|B\rangle$ during each interval. If $T_B \geq T_{\text{int}}/2$, the interval is classified as a click; otherwise, it is classified as no-click. Detection errors are then applied by flipping the click (no-click) outcome with probability p_{FN} (p_{FP}), as obtained from the HMM analysis described in Section 3. Note that a brief excursion to $|B\rangle$ lasting less than $T_{\text{int}}/2$ results in a missed detection even before the detection error is applied. Fig. S8 presents simulation results corresponding to the experimental data in Fig. 3. Panel **a** shows the simulated qubit Z-polarisation conditioned on no clicks. Panel **b** displays the no-click probability $P^{(0)}(\lambda, t)$ and panel **c** summarises the error budget by showing the fraction of trajectories affected by each error type.

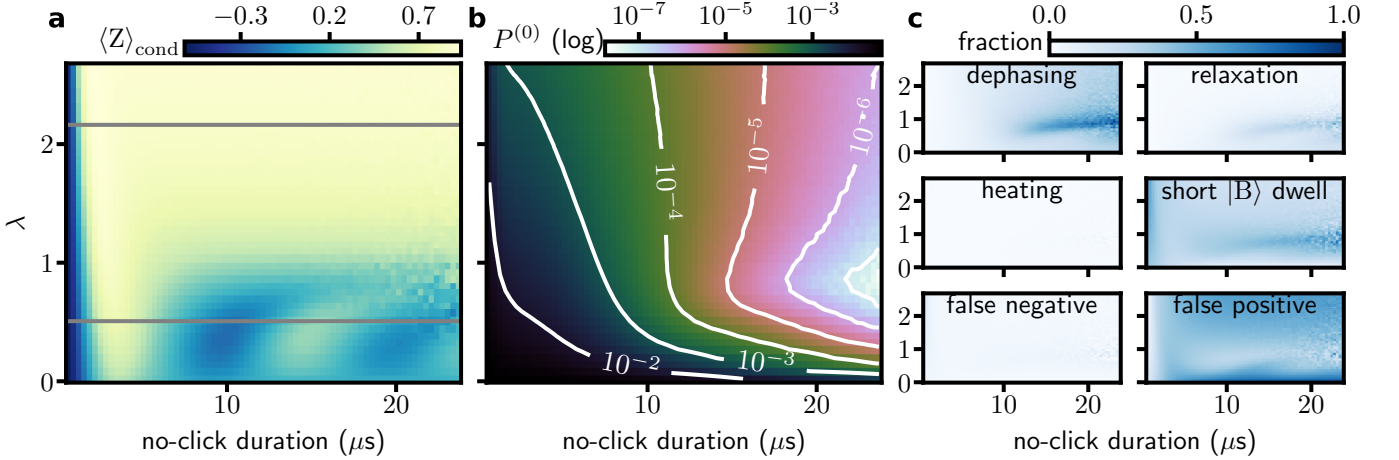


FIG. S8. Numerical simulation of the no-click evolution. **a**, Simulated qubit Z-polarisation as a function of the no-click sequence duration and measurement strength λ . Each pixel corresponds to the average of 3×10^8 stochastic trajectories, though the effective number decreases at longer durations where a click typically occurs during a trajectory (see b). The simulated behaviour is in good agreement with the experimental data (cf. Fig. 3a). The horizontal grey lines indicate the λ -values of the one-dimensional cuts in Fig. 3b — one below the first transition ($\lambda = 0.5$) and one above it ($\lambda = 2.2$). **b**, probability of obtaining no clicks up to time t , $P^{(0)}(\lambda, t)$. Most trajectories experience a click before reaching the target duration. **c**, Error budget. Each panel shows the fraction of trajectories that reached the target duration but experienced an event of the type indicated.

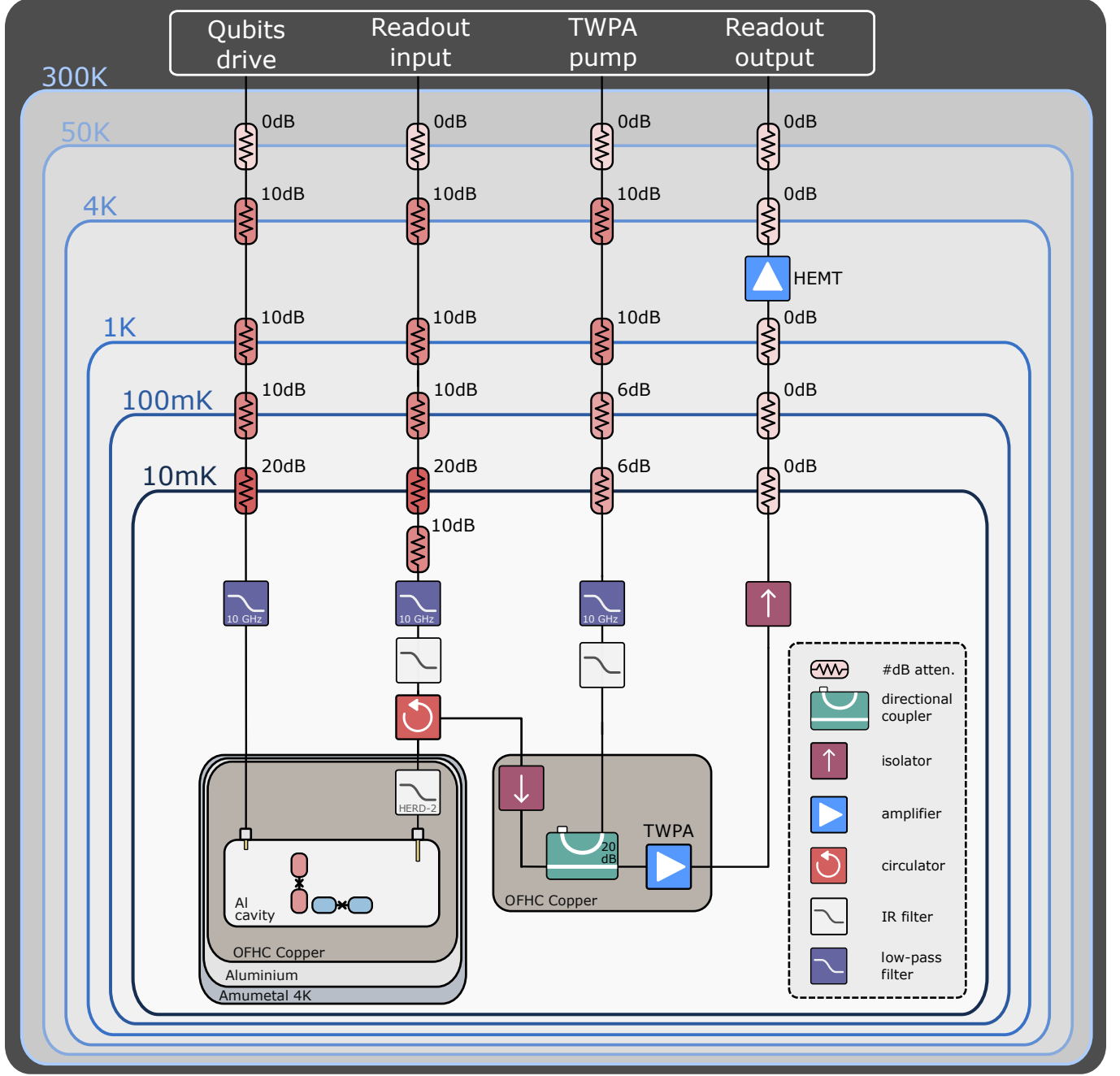


FIG. S9. **Cryogenic microwave wiring diagram.** The experimental device is enclosed within OFHC copper and A4K shields for thermal and magnetic isolation. Control signals are synthesised by a Quantum Machines OPX+ system and upconverted using IQ-mixers before entering the cryostat. They pass through a sequence of attenuators, low-pass filters (LPF), and infrared filters to ensure proper thermalisation and noise suppression. The output signal is first amplified by a travelling-wave parametric amplifier (TWPA, Silent Waves Dreadnought) and then routed through a double-junction isolator, enabling high-fidelity single-shot readout.